Mechanical Systems and Signal Processing 191 (2023) 110158

Contents lists available at ScienceDirect

Mechanical Systems and Signal Processing

journal homepage: www.elsevier.com/locate/ymssp

Maps unlock the full dynamics of targeted energy transfer via a vibro-impact nonlinear energy sink

Ruofeng Liu [a], Rachel Kuske [b,*], Daniil Yurchenko [c]

[a] Computational Applied Mathematics and Operations Research, Rice University, USA
[b] School of Mathematics, Georgia Institute of Technology, Atlanta, USA
[c] ISVR, University of Southampton, UK

ARTICLE INFO

Communicated by X. Jing

Keywords:
Vibro-impact
Targeted energy transfer
Impact map
Nonlinear sink
Bifurcation

ABSTRACT

We consider a model of a vibro-impact nonlinear energy sink (VI-NES), where a ball moves within a cavity of an externally forced mass, impacting either end of the cavity. These impacts result in energy transfer from the mass to the ball, thus limiting the oscillations of the larger system. We develop a semi-analytical map-based approach, recently used for an inclined impact pair model, in the setting where there is energy transfer between the mass and the ball. With this approach we analytically derive exact expressions for the full dynamics of the VI-NES system without restricting the range of parameters, in contrast to other recent work in which an approximate reduced model is valid only for small mass of the ball, small amplitude, and a limited frequency range. We develop the bifurcation analysis for the full VI-NES system, based on exact maps between the states at successive impacts. This analysis yields parameter ranges for complex periodic responses and stability analyses for $O(1)$ mass of the ball, forcing frequencies that are not the same as the natural frequency, and large amplitude forcing. The approach affords the flexibility to analytically study the dynamics of different periodic solutions and their stability, including a variety of impact sequences in the full two degree-of-freedom model of VI-NES. Comparisons of quantities that characterize the energy transfer point to the significance of different types of periodic behavior, which may occur for different parameter combinations. Our semi-analytical results also provide the impact phase, which plays an important role in the efficiency of the energy transfer.

1. Introduction

Recent years have seen increased exploration into new mechanisms of Targeted Energy Transfer (TET), a fundamental phenomenon in the areas of passive vibration control and in energy harvesting. In a general sense TET is an extension of a classical linear tuned mass damper, where a second mass–spring system is added to a primary oscillator to limit its high amplitude vibrations. In the successful implementation of TET, the vibration energy in the primary structure is transferred one-way to the second system, where it can be absorbed by damping or converted to electrical energy, but not fed back to the primary structure. There are many studies of TET in the setting where the coupled system consists of a forced linear oscillator coupled to a Nonlinear Energy Sink (NES), traditionally with a (cubic) nonlinear stiffness and a linear viscous damper. The nonlinearity then provides the opportunity for passive energy transfer while targeting a broad band of frequencies generated from the primary structure; thus it may outperform classical linear dampers through this broadband feature. In fact, the first example where TET was observed was a nonlinear oscillator

* Corresponding author.
E-mail addresses: rl79@rice.edu (R. Liu), rachel@math.gatech.edu (R. Kuske), d.yurchenko@soton.ac.uk (D. Yurchenko).

https://doi.org/10.1016/j.ymssp.2023.110158
Received 23 October 2022; Received in revised form 21 December 2022; Accepted 24 January 2023
Available online 8 February 2023

(with no linear component) attached to a linear system [1]. It was shown that when a linear system was exposed to free vibrations (due to initial velocity) the nonlinear system was able to effectively absorb energy from the linear system under some conditions. However, that study has excluded a linear term in the nonlinear oscillator, so that such a combination was not considered, until recently in [2]. In that work the authors showed that a NES with a combination of linear and nonlinear elements can also be efficient under proper selection of the spring coefficients.

Many of the NES (or TET) studies have been focused on "classical" smooth nonlinear dynamic dampers and absorbers to efficiently mitigate vibrations, see [3–5] and references therein. Within such a classical framework, it is necessary to tune the system in order to take advantage of the frequency range in which the particular nonlinear transfer is effective. Without exact analytical solutions for the classical nonlinear two DOF system, there is not an "obvious" optimal choice for transferring energy from a forced linear oscillator to a nonlinear energy sink via nonlinear coupling. Analyses are generally based on weakly nonlinear approximations or reductions to a two-state system. Parametric studies are limited within these approximations, so that explorations of the full nonlinear behavior rely on simulations, especially if higher degree-of-freedom systems are considered. The recent study [6] provides an extensive reference list on other NES mechanisms, using piecewise nonlinearities, non-linear damping, bistability, inerters, and vibro-impacts.

Recently, there have been several new lines of investigation into the use of vibro-impact (VI) systems in TET, where the impacts provide a source of energy transfer and thus damping, when the restitution coefficient is less than unity. The use of VI suggests a range of TET mechanisms, given the instantaneous TET efficiency achieved on a relatively short time scale [6]. The different mechanisms explored include impacts between two linear damped oscillators [7] and comparisons of impact dampers with tuned mass dampers in [8]. The early concept of an impact damper, where a mass moves between two walls of a container, appeared in [9], with variations on this idea including particle dampers and liquid sloshing dampers [10,11]. A series of papers including [5,6,12,13] and references therein, and [14] provide analytical and experimental explorations of a nonlinear energy sink mechanism termed VI-NES, based on a vibro-impact pair as an impact damper. In this model a ball moves freely within a cavity in a larger forced mass, impacting either end of the cavity. This mechanism is also the focus of this study.

Within VI-NES, the desired TET can be realized on a faster time scale than other NES's, obviously an important feature in efficiently achieving instantaneous vibration control [15]. Results in [16] demonstrate the broad bandwidth of the VI-NES energy transfer, in contrast to the limited bandwidth of classical NES, and apply this advantage to control chatter in a turning application. Current studies reveal that the key point of VI-NES design for vibration damping resides in the relationship between the clearance dimension (size of the cavity) and the vibration level [17], which can be a disadvantage as compared with a NES system with an unrestricted response. Given the (dis)advantages of and differences between VI-TET and classical TET, the choice to use one or the other often depends on the particular application. For example, recognizing the efficiency of the VI-NES design, [18] studies it as the basis for an electromagnetic energy harvesting system.

While promising as a mechanism, the analyses of VI systems have challenges, given the non-smooth dynamics, for which many standard techniques developed for smooth systems do not apply. Analytical work on VI-NES has primarily used the method of multiple scales, adapted from modulation analyses for NES as in [19,20], the validity of which requires the mass of the ball to be much less (e.g. <1% as in [21]), than that of the primary mass. In that limit, [13] observes that the optimal TET response occurs for two impacts per forcing period, where the ball impacts each end of the cavity once per period of the external forcing. Then a reduced system describes the slow modulation of this simple periodic behavior, also studied in [12]. A series of papers by Seguy and Berlioz, et al. uses the asymptotic approach to contrast with the modulation of NES [20] and to explore different response regimes within the slow modulation setting, e.g. in [21,22], including comparison with experiments. Results in [13,17] compare experiments with predictions for the optimal cavity length based on the reduced multiple scale system. There the optimal tuning is based on the resonant frequency. Analysis in [23] identifies Lyapunov exponents for chaotic behavior in the model, demonstrating consistency with those obtained from experiments. Extensions of the multiple scale analysis have been applied to two VINES in parallel [17,24], complemented with experimental comparisons. Recently [25–27] use the asymptotic reduction withing models combining classical NES and impacts, which we discuss further in the Conclusions.

An extensive discussion of the slow modulation approach is given in [14], applying the multiple scale analysis to get explicit expressions for the magnitude of the modulation. They provide backbone curves in the limits of small mass of the ball and excitation frequency near that of the natural frequency of the primary oscillator. Reduced systems based on these limits are studied for an electromagnetic energy harvester [18] and for the TET mechanism using maps in [6]. This latter formulation aims for an improved description of the VI-NES dynamics in the limiting case, and an understanding of the potential use of VI-NES both for energy harvesting and TET. These analyses provide value for understanding energy absorption via a light mass, for simple periodic behavior under forcings with small amplitude and frequencies near the natural frequency, A larger range of parameters is of interest in studying realistic systems, which may have unanticipated influence on TET as we illustrate for some typical energy measures. Thus, the analysis based on an exact solution provides the opportunity to explore behavior outside of small forcing and in the context of other forcing frequencies. It affords one the luxury to consider any combination of parameter values, since we have the exact expression for the impact dynamics.

Analytical studies of VI-NES-type models point to other gaps in the study of impacting systems, as discussed in detail in a recent study of bifurcations of the impact pair-type energy harvester [28]. While there have been extensive studies of bifurcations in single degree of freedom (SDOF) VI systems, such as a forced mass and motionless rigid barrier(s) or a bouncing ball on an oscillating surface [29], there are far fewer analyses of impacts in two or higher degree of freedom systems. These include, e.g., a pair of moving impacting masses, either of which can be forced. Results based on the canonical impact pair [10,30–32] are based on the assumption that the mass of the ball is negligible relative to that of the larger mass of the capsule, and therefore do not capture

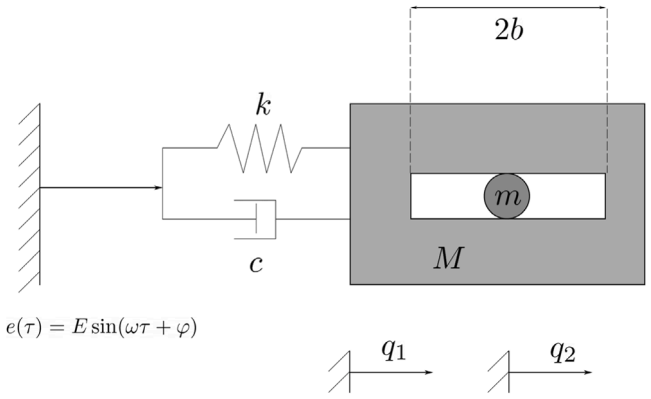

Fig. 1. A linear oscillator with a small mass inside the cavity.

the energy transfer aspects of the VI-NES system. Nevertheless, recent success in exploring stability and bifurcations of complex behavior in impact-pair-type energy harvesting indicates new approaches for studying VI-NES.

Recent works [30,32] utilize maps between impacts in the context of the horizontal impact pair, and for the inclined case for a VI energy harvester (VI-EH) based on an inclined impact pair, yielding analytical results for the relative motion between ball and capsule. Inspired by these previous results that capture bifurcations and stability semi-analytically, here we develop the bifurcation analysis for the full VI-NES system, deriving maps between the states at successive impacts. While the approach has some similarities to the use of Poincaré maps, it differs in that the maps are based on states at different stages, i.e. multiple impacts, within a forcing period [30]. This approach allows us to find arbitrarily complex periodic responses and to perform stability analyses analytically.

By adapting the map-based approach to the full VI-NES system, we provide the flexibility to consider different types of periodic solutions that include any possible combination of impact sequences in the full two DoF model of VI-NES. Conceptually this mirrors the treatment in [32] for the relative dynamics, but in the VI-NES context this approach must handle the maps in terms of the absolute dynamics of both small and large masses, given the feedback between the masses at impact. The method does not depend on limitations on the parameter ranges, and thus can be used to explore behavior for $O(1)$ mass of the ball, forcing frequencies that are not the same as the natural frequency, and large amplitude forcing. Comparisons of energy transfer measures point to the significance of different types of periodic behavior, which may occur for different parameter combinations. Here, we also see the importance of impact phase on the energy transfer, with this impact phase provided in the semi-analytical results for the full VI-NES system.

The structure of the paper is as the follows: In Section 2, we present the VI-NES model and governing equations of motion. In Section 3 we derive our analytical map-based treatment, applying it to the VI-NES system in Section 4 to obtain the bifurcation and stability results for different periodic solutions. In Section 5 the analytical result and numerical results are compared. In Section 6 we compare different types of periodic and complex behavior by considering the corresponding energy transfer, based on two different measures.

2. The model

The model of interest, as discussed in [14] is composed of a linear oscillator (LO) with mass M and a vibro-impact nonlinear energy sink (VI-NES) via a ball of mass m that can slide without friction inside a cavity of length $2b$ inside the LO. The primary mass of the LO is subject to a harmonic base excitation $e(\tau) = E\sin(\omega\tau)$ with a period $2\pi/\omega$, illustrated in Fig. 1 by a spring with linear stiffness k and damping coefficient c. Taking q_1 and q_2 as the absolute positions of the center of the cavity in the LO and of the ball, respectively, the motion between impacts ($|q_1 - q_2| < b$) of the LO and the ball is smooth and is governed by equations

$$Mq_1'' + cq_1' + kq_1 = kE\sin(\omega\tau + \varphi) + c\omega E\cos(\omega\tau + \varphi) \tag{1}$$

$$q_2'' = 0\,. \tag{2}$$

Here φ indicates a phase shift of the forcing, relative to an initial time $t = 0$. In general we do not consider the initial value problem for this system, as we are interested in long time behavior and the corresponding attracting behavior for inelastic impacts. However, when considering periodic solutions, the phase shift φ relative to the impact times is of interest as discussed in the following sections.

Impacts between the LO and the ball occur when $|q_1 - q_2| = b$, and their dynamics is governed by the instantaneous Newtonian impact law and conservation of momentum

$$(q_1'^{+} - q_2'^{+}) = -r(q_1'^{-} - q_2'^{-}) \tag{3}$$

$$Mq_1'^{+} + mq_2'^{+} = Mq_1'^{-} + mq_2'^{-}\,, \tag{4}$$

Table 1
Model parameters and their values, as in [14].

Parameter description	Value
Mass of LO	$M = 3.807$ kg
Damping coefficient	$c = 2.53$ Ns/m
Linear stiffness coefficient	$k = 11680$ N/m
Natural frequency	$\omega_0 = 55.39$
Half cavity length	$b = .015$ m
Non-dimensionalized damping coefficient	$\lambda = 0.01199$
Restitution coefficient	$r = 0.65$

where r is the coefficient of restitution and the superscripts $(\cdot)^-, (\cdot)^+$ denote the variable immediately before and after the impact, respectively. In (1)–(4), $(\cdot)'$ indicates $\frac{d}{d\tau}$.

We rewrite (1)–(4) in terms of non-dimensionalized variables to facilitate the analysis. The non-dimensionalized displacements are x_1, and x_2, which are obtained by scaling the variables q_1, q_2 by the half-length of the cavity,

$$x_1 = \frac{q_1}{b}, \quad x_2 = \frac{q_2}{b}\,. \tag{5}$$

Likewise, the following changes of variables yield non-dimensionalized parameters for the ratio of the masses, strength of the forcing, natural frequency, ratio of frequencies, and damping, respectively.

$$\mu = \frac{m}{M}, \quad A = \frac{E}{b}, \quad \omega_0 = \sqrt{\frac{k}{M}}, \quad \Omega = \frac{\omega}{\omega_0}, \quad \lambda = \frac{c}{M\omega_0}\,. \tag{6}$$

Here we define λ analogously to that in [14,22], with M rather than m in the denominator so that no factor of μ appears in the non-dimensional damping coefficient. Moreover, we use the dimensionless time t, obtained by scaling with the natural frequency of the LO,

$$t = \omega_0 \tau\,. \tag{7}$$

Substituting (6)–(7) into Eqs. (1)–(4) gives the non-dimensionalized equations of motion and corresponding impact conditions,

$$\begin{aligned} |x_1 - x_2| < 1 \,:\; & \ddot{x}_1 + \lambda\dot{x}_1 + x_1 = A\sin(\Omega t + \varphi) + \lambda\Omega A\cos(\Omega t + \varphi) \\ & \ddot{x}_2 = 0 \end{aligned} \tag{8}$$

$$\begin{aligned} |x_1 - x_2| = 1 \,:\; & \dot{x}_1^+ - \dot{x}_2^+ = -r(\dot{x}_1^- - \dot{x}_2^-) \\ & \dot{x}_1^+ + \mu\dot{x}_2^+ = \dot{x}_1^- + \mu\dot{x}_2^-\,, \end{aligned} \tag{9}$$

with $\dot{}$ indicating $\frac{d}{dt}$. The damping coefficient λ is assumed to satisfy $\lambda^2 - 4 < 0$, so that the characteristic equation for the homogeneous equation for x_1 in (8) has two conjugate complex roots, yielding oscillatory dynamics.

The time series and phase planes shown in Fig. 2 illustrate several types of periodic behaviors for the system (1). There we show both the absolute displacement of the ball and cavity, as well as the relative displacement w and relative velocity $\dot{w}$,

$$w = x_1 - x_2, \qquad \dot{w} = \dot{x}_1 - \dot{x}_2\,. \tag{10}$$

The left column illustrates the motion of the ball within the cavity. The middle column shows the relative displacement w and relative velocity $\dot{w}$ corresponding to the time series in the left column. The right column shows the dynamics of the trajectory in the $w - \dot{w}$ phase plane, from which it is clear that behaviors are periodic. In the phase plane the vertical lines indicate the application of the impact condition when the ball reaches the end of the cavity. Following [32], we find it useful to introduce the notation n:m/pT to refer to periodic solutions with n impacts on the left and m impacts on the right of the cavity in a time interval pT, for T the period of the external forcing. In the following, for $p = 1$, we drop the T; e.g., 1:1 refers to a solution with alternating impacts on the left and right ends of the cavity, with two impacts per forcing period T. Then Fig. 2 shows a symmetric 1:1 solution in (a)–(c), asymmetric 1:1 solution in (d)–(f), 1:1/2T solution in (g)–(i) and 2:1 solution in (j)–(l).

The analyses of [6] and [14] focus on the symmetric 1:1 solution for $\mu = m/M \ll 1$ near $\Omega \sim 1$. In our analysis, we provide an approach that captures different periodic solutions and their stability for a range of parameters beyond small μ and $\Omega \sim 1$. As indicated in Table 1, throughout the paper we use the same parameter values for M, c, k, and b as in [14]. In contrast to their analysis, below we consider larger ranges of E, m, and ω, together with small and $O(1)$ values of A, the non-dimensionalized forcing amplitude (6).

The solutions plotted in Figs. 2(a)–(l) are obtained by solving system (8) using a fourth-order Runge–Kutta algorithm for the smooth evolution of the system. A sufficiently small time step h is used to ensure the accuracy of the solution. When an impact is detected, as indicated by the ball exiting the cavity, $|x_1 - x_2| > 1$, the previous step is rejected and h is reduced by a factor of two. We use this bisection procedure to find the time of the impact within an error of $\epsilon < 10^{-9}$. Below we obtain semi-analytical results for periodic solutions, comparing to the numerical solutions for a range of m, ω, and E, thus illustrating the flexibility of the approach.

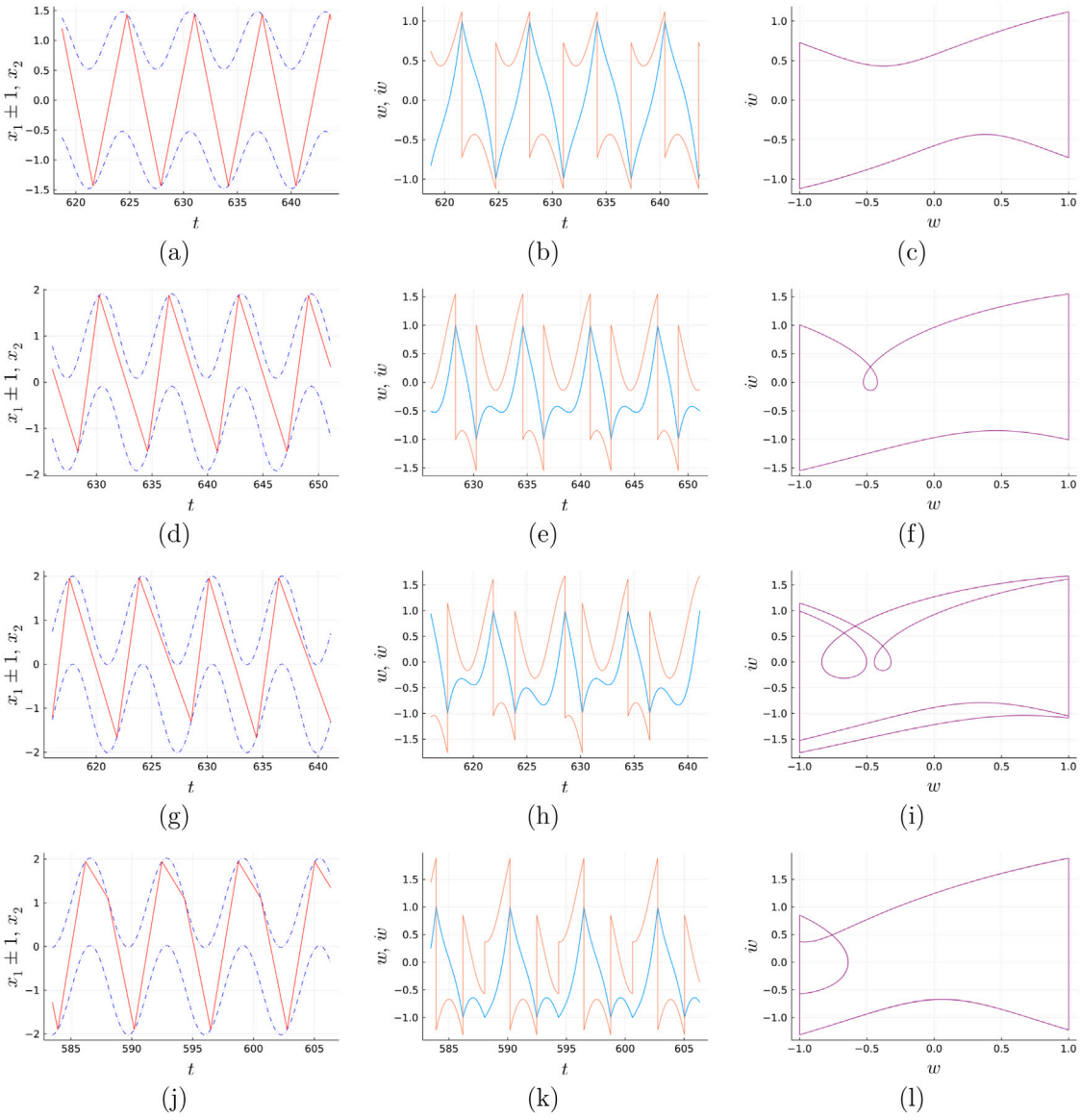

Fig. 2. Representative time series and phase planes of stable periodic solutions. Left column: time series for the displacement of left and right cavity ends (dotted blue lines) and ball (red solid line). Middle Column: Corresponding relative displacement w (blue) and relative velocity $\dot{w}$ (red); Right column: Corresponding phase plane of w vs. $\dot{w}$. (a)–(c) $A = 0.015$; (d)–(f) $A = 0.020$; (g)–(i) $A = 0.021$; (j)–(l) $A = 0.023$. For all plots, $\Omega = 1(\omega = \omega_0)$, $\mu = .0084$ ($m = .032$ kg), with the remaining parameters provided in Table 1. (For interpretation of the references to color in this figure legend, the reader is referred to the web version of this article.)

2.1. Energy transfer measures

The energy transfer that takes place via a TET mechanism can be characterized by a variety of measures, as can be found throughout the literature, e.g. as in [7,18], and [13]. The focus in [14] is on the response of a 1:1 symmetric periodic solution near resonance, considering backbone curves for the system amplitude. Likewise, we consider the amplitude of the system response given by $\max|x_1|$. To provide a complementary perspective on the efficiency of TET, we include an additional quantity: the ratio of the average kinetic energy for both masses, that is,

$$K_2/K_1, \quad \text{where} \quad K_1 = \langle M\dot{x}_1^2 \rangle, \qquad K_2 = \langle m\dot{x}_2^2 \rangle . \tag{11}$$

This ratio increases if more energy is transferred from the LO to the ball. Here the average is taken over a sufficiently large time interval, depending on whether the behavior is chaotic or periodic.

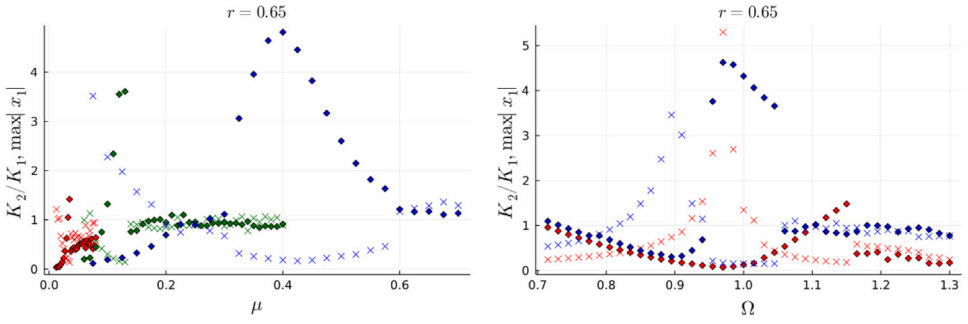

Fig. 3. Examples of K_2/K_1 (diamonds) and $\max|x_1|$ (×'s) vs. μ and vs. Ω, showing behavior of the system away from $\mu \ll 1$ and $\Omega = 1$. Left: $\Omega = 1$ and $A = .03$ (red markers), $A = 0.1$ (green), and $A = 0.3$ (blue); Zoomed in figures for $A = .03$ show more detail in Fig. 8. Right: $\mu = .05$, $A = .1$ (red markers) and $\mu = .2$, $A = .15$ (blue). Other parameters are as in Table 1, unless otherwise indicated in the figures. (For interpretation of the references to color in this figure legend, the reader is referred to the web version of this article.)

Fig. 3 shows the variability of K_2/K_1 (diamonds) and $\max|x_1|$ (×) for $\mu = O(1)$ and $\Omega \neq 0$. These illustrate parameter ranges where different behaviors of interest – e.g. K_2/K_1 larger and $\max|x_1|$ small – occur away from $\mu \ll 1$ and $\Omega = 1$, thus motivating the need for analysis of the dynamic behavior away from these limits. Further discussion of the energy transfer measures, in the context of the analytical results and for different values of r, is in Section 6.

As an aside, we note that not all TET energy transfer measures are appropriate for the VI-NES system. For example, the measure considered in [7] for two impacting discrete linear oscillators is based on the sum of differences in kinetic energy for the second oscillator, after and before impact. In the context of the VI-NES system, such a sum telescopes to a trivial result, and thus does not capture the behavior over a relevant time interval.

3. Analysis via maps

A natural approach for efficiently tracking the state of the system is to express the dynamics in terms of the state at impact. We denote $x^-_{j,k}$, $x^+_{j,k}$ ($\dot{x}^-_{j,k}$, $\dot{x}^+_{j,k}$) as the displacement (velocity) of mass $j = 1,2$ immediately before and after the kth impact, respectively. The time of the kth impact is given by t_k. Together with continuity of displacement at impact, the linear system of impact conditions (9) is rewritten with $\dot{x}^+_{j,k}$ expressed in terms of $\dot{x}^-_{j,k}$,

$$\begin{aligned} &x^-_{j,k} = x^+_{j,k} \qquad j = 1,2\,, \qquad x_{1,k} - x_{2,k} = 1(-1) \qquad \text{on } L\ (R) \\ &\dot{x}^+_{1,k} = \frac{1-r\mu}{1+\mu}\dot{x}^-_{1,k} + \frac{r\mu+\mu}{1+\mu}\dot{x}^-_{2,k}\,, \qquad \dot{x}^+_{2,k} = \frac{1+r}{1+\mu}\dot{x}^-_{1,k} + \frac{\mu-r}{1+\mu}\dot{x}^-_{2,k}\,. \end{aligned} \tag{12}$$

where L (R) indicates the left(right) cavity end. Our goal is to track the system in terms of the state vector

$$\mathbf{s}_k = (x_{1,k}, \dot{x}_{1,k}, x_{2,k}, \dot{x}_{2,k}, t_k)\,, \qquad x_{j,k} \equiv x^-_{j,k}\,, \quad \dot{x}_{j,k} \equiv \dot{x}^-_{j,k}\,, \tag{13}$$

a tuple of the five variables that completely describes the state of system immediately before the kth impact. Here we drop the superscript "−" in the definition of $\mathbf{s}_k$ and throughout the rest of the paper, since we can use the expressions above to write the system in terms of $x^-_{2,k}, \dot{x}^-_{2,k}$ only. Specifically, we solve the linear ODEs (8) for the dynamics in-between impacts to obtain explicit formula for $x^+_{j,k-1}, \dot{x}^+_{j,k-1}$ in terms of $x^-_{j,k}, \dot{x}^-_{j,k}$, for $j = 1,2$. For example, integrating (8) (twice) yields

$$\dot{x}^-_{2,k} = \dot{x}^+_{2,k-1} \qquad x^-_{2,k} = x^+_{2,k-1} + \dot{x}^+_{2,k-1}(t_k - t_{k-1}) \tag{14}$$

Then, from (12) and (14), we obtain $\dot{x}^-_{2,k}$ and $x^-_{2,k}$ in terms of $x^-_{j,k-1}, \dot{x}^-_{j,k-1}$ only, which we use in the remainder of the calculations. The same procedure is used for $j = 1$, likewise eliminating $x^+_{1,k}, \dot{x}^+_{1,k}$. Using (13), we have the basis for four different maps P_j for the transition $\mathbf{s}_{k-1} \to \mathbf{s}_k$, capturing the motion of the ball between two consecutive impacts,

$$P_1 : \mathbf{s}_{k-1} \to \mathbf{s}_k \text{ for } L \mapsto R, \qquad P_2 : \mathbf{s}_{k-1} \to \mathbf{s}_k \text{ for } R \mapsto L \tag{15}$$

$$P_3 : \mathbf{s}_{k-1} \to \mathbf{s}_k \text{ for } L \mapsto L, \qquad P_4 : \mathbf{s}_{k-1} \to \mathbf{s}_k \text{ for } R \mapsto R\,, \tag{16}$$

where L and R indicate the left and right ends of the cavity.

Integrating (8) and combining with (9) and the expressions for $x^+_{j,k}, \dot{x}^+_{j,k}$ discussed above, yields the same form for all of the maps P_j,

$$\begin{aligned} x_{1,k} &= a_{1,k-1}e^{\frac{-\lambda t_k}{2}}\sin(\gamma t_k) + a_{2,k-1}e^{\frac{-\lambda t_k}{2}}\cos(\gamma t_k) + b_1\sin(\Omega t_k + \varphi) + b_2\cos(\Omega t_k + \varphi) \\ &\equiv \mathcal{G}(t_{k-1}, t_k, x_1, \dot{x}_{1,k-1}, \dot{x}_{2,k-1}, \varphi) \\ \dot{x}_{1,k} &= a_{1,k-1}e^{\frac{-\lambda t_k}{2}}\left(-\frac{\lambda}{2}\sin(\gamma t_k) + \gamma\cos(\gamma t_k)\right) + a_{2,k-1}e^{\frac{-\lambda t_k}{2}}\left(-\frac{\lambda}{2}\cos(\gamma t_k) - \gamma\sin(\gamma t_k)\right) \end{aligned} \tag{17}$$

$$+ b_1\Omega\cos(\Omega t_k+\varphi) - b_2\Omega\sin(\Omega t_k+\varphi) \equiv \mathcal{H}(t_{k-1}, t_k, x_1, \dot{x}_{1,k-1}, \dot{x}_{2,k-1}, \varphi) \tag{18}$$

$$x_{2,k} = x_{2,k-1} + \left(\frac{1+r}{1+\mu}\dot{x}_{1,k-1} + \frac{\mu-r}{1+\mu}\dot{x}_{2,k-1}\right)\cdot(t_k - t_{k-1}) \tag{19}$$

$$\dot{x}_{2,k} = \frac{1+r}{1+\mu}\dot{x}_{1,k-1} + \frac{\mu-r}{1+\mu}\dot{x}_{2,k-1}\,, \tag{20}$$

where

$$\gamma = \sqrt{1-\left(\frac{\lambda}{2}\right)^2}, \quad b_1 = \frac{\begin{vmatrix} A & -\lambda\Omega \\ A\lambda\Omega & 1-\Omega^2 \end{vmatrix}}{\begin{vmatrix} 1-\Omega^2 & -\lambda\Omega \\ \lambda\Omega & 1-\Omega^2 \end{vmatrix}}, \quad b_2 = \frac{\begin{vmatrix} 1-\Omega^2 & A \\ \lambda\Omega & A\lambda\Omega \end{vmatrix}}{\begin{vmatrix} 1-\Omega^2 & -\lambda\Omega \\ \lambda\Omega & 1-\Omega^2 \end{vmatrix}}.$$

The functions $\mathcal{G}$ and $\mathcal{H}$ are introduced for convenience, with their arguments highlighting the dependence of the coefficients $a_{1,k-1}$, $a_{2,k-1}$ on $x_{1,k-1}, \dot{x}_{1,k-1}, \dot{x}_{2,k-1}, t_{k-1}$. They appear in the system of equations for $x_{1,k-1}, \dot{x}_{1,k-1}$ when solving the equations for the LO dynamics in (8) and applying the impact condition (9), specifically,

$$\begin{aligned} &e^{-\frac{\lambda t_{k-1}}{2}}\begin{bmatrix} \sin(\gamma t_{k-1}) & \cos(\gamma t_{k-1}) \\ -\frac{\lambda}{2}\sin(\gamma t_{k-1}) + \gamma\cos(\gamma t_{k-1}) & -\frac{\lambda}{2}\cos(\gamma t_{k-1}) - \gamma\sin(\gamma t_{k-1}) \end{bmatrix}\begin{bmatrix} a_{1,k-1} \\ a_{2,k-1} \end{bmatrix} \\ &\quad = \begin{bmatrix} x_{1,k-1} \\ \frac{1-r\mu}{1+\mu}\dot{x}_{1,k-1} + \frac{r\mu+\mu}{1+\mu}\dot{x}_{2,k-1} \end{bmatrix} - \begin{bmatrix} b_1\sin(\Omega t_{k-1}+\varphi) + b_2\cos(\Omega t_{k-1}+\varphi) \\ b_1\Omega\cos(\Omega t_{k-1}+\varphi) - b_2\Omega\sin(\Omega t_{k-1}+\varphi) \end{bmatrix}. \end{aligned} \tag{21}$$

In order to complete the evaluation of $\mathbf{s}_k$ from $\mathbf{s}_{k-1} = (x_{1,k-1}, \dot{x}_{1,k-1}, x_{2,k-1}, \dot{x}_{2,k-1}, t_{k-1})$ using (17)–(20), the value of t_k is needed, as well as conditions specific to each of the maps P_j. We use the known information at impact, namely,

$$x_{1,\ell} - x_{2,\ell} = \pm 1, \qquad \text{for all } \ell\,. \tag{22}$$

Note that the choice of ± 1 for $\ell = k$ and $\ell = k-1$ provides the distinction among the maps P_j for $j = 1, 2, 3, 4$: for P_2 and P_3, $x_{1,k} - x_{2,k} = 1$ and $x_{1,k-1} - x_{2,k-1} = 1(-1)$ for P_2 (P_3). Likewise, for P_1, P_4, $x_{1,k} - x_{2,k} = -1$ and $x_{1,k-1} - x_{2,k-1} = 1(-1)$ for P_1 (P_4). With the appropriate values for $x_{1,\ell} - x_{2,\ell}$ from (22) for $\ell = k, k-1$, together with the initial values in $\mathbf{s}_{k-1}$, the system (17)–(20) yields a system of four equations from which we determine the remaining four unknowns $(x_{1,k}, \dot{x}_{1,k}, \dot{x}_{2,k}, t_k)$ specific to P_j.

We note that with these maps as building blocks, we can study a range of different periodic behaviors via compositions of the various P_j. Then this analysis can consider behaviors beyond the simple 1:1 behavior, on which the approximations used in [12,19,21] and [6,18] are based.

4. Analytical results

We provide analysis for periodic solutions with the same period T as that of the forcing function in (8). These solutions represent behavior that is attracting for periodic forcing and for $r < 1$. In that case there is sufficient dissipation in the system so that for large ranges of the parameter values, the dynamics tend toward periodic behavior. Our analysis provides analytical results for the parameter values corresponding to these periodic solutions, also determining their linear stability.

4.1. Periodic solutions: 1:1

We first focus on the 1:1 periodic solution, with periodicity conditions

$$t_{k-1} + T = t_{k+1}, \quad x_{j,k-1} = x_{j,k+1}, \quad \dot{x}_{j,k-1} = \dot{x}_{j,k+1}, \qquad j = 1, 2\,. \tag{23}$$

Then these 1:1 periodic solutions are characterized by impacts on alternating ends of the cavity where $\mathbf{s}_{k-1} = \mathbf{s}_{k+1}$, with the understanding that t_{k-1} and t_{k+1} are equal in the mod T sense, as in (23). Written in terms of the maps, periodicity of the 1:1 solution is $P_2(P_1(\mathbf{s}_{k-1})) = \mathbf{s}_{k+1}$. Using the intermediate state variable $\mathbf{s}_k$, the equations for the periodic 1:1 solution are

$$\mathbf{s}_{k-1} = P_2(\mathbf{s}_k) = \mathbf{s}_{k+1}\,, \qquad \text{where} \quad P_1(\mathbf{s}_{k-1}) = \mathbf{s}_k, \qquad t_{k+1} - t_{k-1} = T\,. \tag{24}$$

Then, as described above, using (17)–(20) together with (22) for P_1 and P_2 we have systems of equations for the remaining unknowns $(x_{1,\ell}, \dot{x}_{1,\ell}, \dot{x}_{2,\ell}, t_\ell)$ for $\ell = k, k+1$ in terms of $\mathbf{s}_{k-1}$. Since we are interested in periodic solutions where $\mathbf{s}_{k-1} = \mathbf{s}_{k+1}$, and $t_{k+1} = t_{k-1} + T$, then we rewrite the system (17)–(20) for P_j in terms of the state variables $\mathbf{s}_k, \mathbf{s}_{k-1}$. Including (9) and (23) as impact and periodic conditions, the system for the 1:1 periodic solution is

$$x_{1,k} = \mathcal{G}(t_{k-1}, t_k, x_{1,k-1}, \dot{x}_{1,k-1}, \dot{x}_{2,k-1}, \varphi) \tag{25}$$

$$\dot{x}_{1,k} = \mathcal{H}(t_{k-1}, t_k, x_{1,k-1}, \dot{x}_{1,k-1}, \dot{x}_{2,k-1}, \varphi) \tag{26}$$

$$x_{2,k} = x_{2,k-1} + \left(\frac{1+r}{1+\mu}\dot{x}_{1,k-1} + \frac{\mu-r}{1+\mu}\dot{x}_{2,k-1}\right)\cdot(t_k - t_{k-1}) \tag{27}$$

$$\dot{x}_{2,k} = \frac{1+r}{1+\mu}\dot{x}_{1,k-1} + \frac{\mu-r}{1+\mu}\dot{x}_{2,k-1} \tag{28}$$

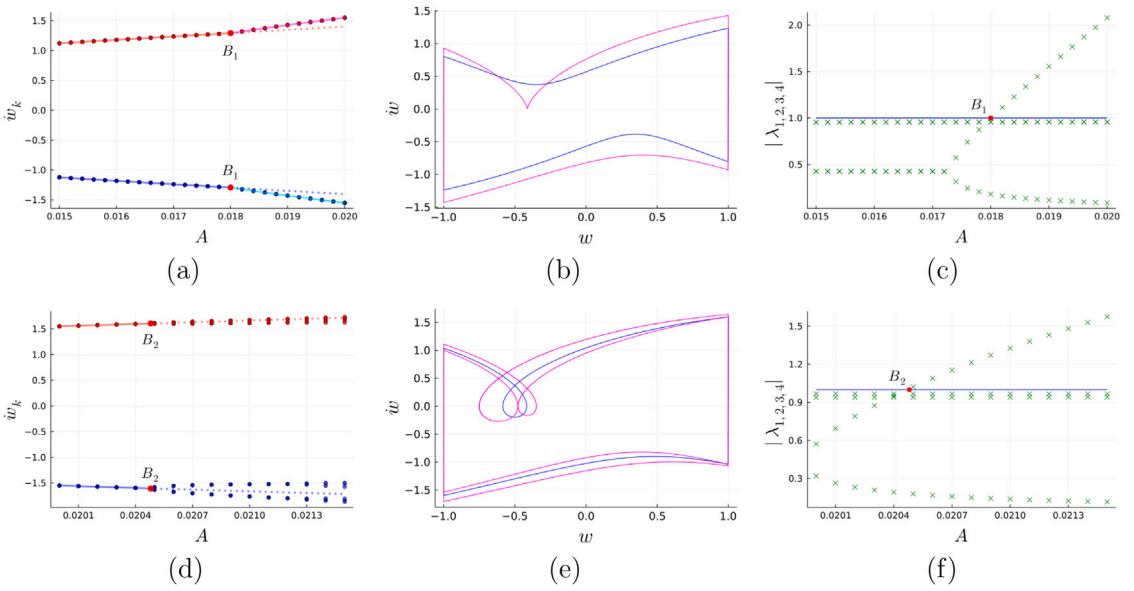

Fig. 4. (a),(d): Bifurcation diagrams of the relative impact velocity $\dot{w}$ vs. A. Red and blue dots show $\dot{w}$ on L and R, respectively, from the numerical simulation of (1)–(4). The red and blue (magenta and cyan) lines in (a) show the analytically obtained symmetric (asymmetric) 1:1 solutions, with B_1 indicating the saddle node bifurcation. In (d) red and blue lines show the analytically obtained asymmetric 1:1 solution, with B_2 indicating the period doubling bifurcation. Numerical results also shown for 1:1/2T solutions. Solid(dotted) lines in (a),(d) show the stable (unstable) solutions. Panels (b),(e): Phase planes showing relative displacements and velocities for solutions on either side of the bifurcations: in (b), symmetric 1:1 solution for $A = .017$ (blue) and asymmetric 1:1 for $A = .019$ (magenta), and in (e), asymmetric 1:1 solution for $A = .0204$ (blue) and 1:1/2T for $A = 0.207$ (magenta). Panels (c),(f): Modulus of the four eigenvalues of $J_{P_2} J_{P_1}$ vs. A. In (c): the eigenvalues for the 1:1 symmetric solution shown in (a); In (f): eigenvalues for the asymmetric 1:1 solution shown in (d). The horizontal blue line is $|\lambda| = 1$ for reference. For B_1 one $\lambda_i > 1$, and for B_2 one $\lambda_i < -1$. (For interpretation of the references to color in this figure legend, the reader is referred to the web version of this article.)

$$x_{1,k} - x_{2,k} = -1 \qquad x_{1,k-1} - x_{2,k-1} = 1 \tag{29}$$

$$x_{1,k-1} = \mathcal{G}(t_k, t_{k+1}, x_{1,k}, \dot{x}_{1,k}, \dot{x}_{2,k}, \varphi) \tag{30}$$

$$\dot{x}_{1,k-1} = \mathcal{H}(t_k, t_{k+1}, x_{1,k}, \dot{x}_{1,k}, \dot{x}_{2,k}, \varphi)$$

$$x_{2,k-1} = x_{2,k} + \left(\frac{1+r}{1+\mu} \dot{x}_{1,k} + \frac{\mu - r}{1+\mu} \dot{x}_{2,k} \right) \cdot (t_{k+1} - t_k)$$

$$\dot{x}_{2,k-1} = \frac{1+r}{1+\mu} \dot{x}_{1,k} + \frac{\mu - r}{1+\mu} \dot{x}_{2,k} \tag{31}$$

$$t_{k+1} = t_{k-1} + T\,. \tag{32}$$

Without loss of generality, in seeking a T-periodic solution we take $t_{k-1} = 0$. Then we solve for the initial values $\mathbf{s}_{k-1}$ on the left cavity end that define the 1:1 periodic solution, with the values $\mathbf{s}_k$ determined from (25)–(29) and the periodic condition (32). Note that we also obtain the phase shift φ written in terms of the impact phase for the 1:1 periodic solution, with $\varphi_{k-1} = \mod(\varphi, 2\pi)$ for $t_{k-1} = 0$. Symmetric (asymmetric) 1:1 solutions are characterized by $\Delta t_{k-1} = \Delta t_k$ ($\Delta t_{k-1} \neq \Delta t_k$), where Δt_i is the time between the ith impact and the $i+1$st impact. Fig. 4 shows the analytical results for 1:1, indicating both symmetric and asymmetric 1:1 solutions.

Fig. 4 compares the analytical and numerical results for the relative impact velocity $\dot{w}_k = \dot{x}_{1,k} - \dot{x}_{2,k}$ of the 1:1 solution by plotting the bifurcation diagram for $\dot{w}_k$ in terms of the parameter A. The numerically obtained bifurcation branches for $\dot{w}_k$, indicated by red and blue dots, are obtained from a continuation-type method. That is, given a value A, the system (1)–(4) is run for a sufficiently long time to reach an attracting solution. This solution is then used as an initial condition for the solution at the next value of A, typically chosen near the previous one. Then the numerical results in Fig. 4 indicate the relative impact velocity $\dot{w}_k$ for the attracting or stable behavior. Fig. 4(a),(d) shows excellent agreement between the numerics and the stable 1:1 solutions determined analytically from (25)–(32). Note that the analytical results for the 1:1 solutions include both stable and unstable solutions, indicated by solid and dotted lines, respectively. Panels (b),(e) show sample stable periodic solutions in the phase plane for parameter combinations on either side of the bifurcations. Consistent with the bifurcations shown in Panels (a), (d), Panels (c),(f) show the eigenvalues for 1:1 solutions, providing conditions for the loss of stability of the 1:1 solution and shown in Section 4.2.

4.2. Linear stability analysis

While the analyses above provide systems of equations for 1:1 solutions, we are not guaranteed that these solutions are stable. Such information is desirable for predictability and sustained energy transfer. We provide a linear stability analysis for the periodic

solutions, which indicates whether small deviations from the periodic behavior decay over time. We give the linear stability analysis for the 1:1 solution, by considering a fixed point given by the vector $\mathbf{S}^*_{1:1} = (\mathbf{s}^*_1, \mathbf{s}^*_2)$ of the map $P_2 \circ P_1$, where $\mathbf{s}^*_1$ ($\mathbf{s}^*_2$) gives the state at impact on L (R). Then, we consider consecutive states at impact, such that

$$\mathbf{s}^*_1 = \mathbf{s}_{k-1} = P_2(P_1(\mathbf{s}_{k-1})) = \mathbf{s}_{k+1}, \quad P_1(\mathbf{s}^*_1) = \mathbf{s}^*_2 = \mathbf{s}_k, \quad \text{with } t_{k-1} = \text{mod}(t_{k+1}, T), \tag{33}$$

together with a small perturbation $\delta\mathbf{s}_{k-1}$ to $\mathbf{s}_{k-1}$. Linearizing about $\delta\mathbf{s}_j = 0$, for $j = k-1, k, k+1$, and using the properties of $\mathbf{s}_{k-1}$ and $\mathbf{s}_k$ in (33), the equation for $\delta\mathbf{s}_{k+1}$, is

$$\begin{aligned} \mathbf{s}_{k+1} + \delta\mathbf{s}_{k+1} &= P_2(P_1(\mathbf{s}_{k-1} + \delta\mathbf{s}_{k-1})) \approx P_2(P_1(\mathbf{s}^*_1) + J_{P_1}(\mathbf{s}^*_1)\delta\mathbf{s}_{k-1}) \\ &\approx P_2(P_1(\mathbf{s}^*_1)) + J_{P_2}(\mathbf{s}_k)J_{P_1}(\mathbf{s}^*_1)\delta\mathbf{s}_{k-1} = P_2(\mathbf{s}^*_2) + J_{P_2}(\mathbf{s}^*_2)J_{P_1}(\mathbf{s}^*_1)\delta\mathbf{s}_{k-1} \\ \implies \delta\mathbf{s}_{k+1} &\approx J_{P_2}(\mathbf{s}^*_2)J_{P_1}(\mathbf{s}^*_1)\delta\mathbf{s}_{k-1} \end{aligned} \tag{34}$$

where J_{P_1}, J_{P_2} are the Jacobian matrices of P_1 and P_2, respectively. Specifically, the J_{P_j} are 4×4 matrices, whose entries are in terms of four of the variables from $\mathbf{s}_{k-m+j}$ for $m = 1, 2$. This form follows from the definition of impact, that is, $x_{1,k} - x_{2,k} = \pm 1$, so that $x_{1,k}$ is written in terms of $x_{2,k}$ to simplify some of the expressions. Then each J_{P_j} takes the form

$$J_{P_j} = \begin{bmatrix} \frac{\partial \dot{x}_{1,k-1+j}}{\partial \dot{x}_{1,k-2+j}} & \frac{\partial \dot{x}_{1,k-1+j}}{\partial \dot{x}_{2,k-2+j}} & \frac{\partial \dot{x}_{1,k-1+j}}{\partial x_{2,k-2+j}} & \frac{\partial \dot{x}_{1,k-1+j}}{\partial t_{k-2+j}} \\ \frac{\partial \dot{x}_{2,k-1+j}}{\partial \dot{x}_{1,k-2+j}} & \frac{\partial \dot{x}_{2,k-1+j}}{\partial \dot{x}_{2,k-2+j}} & \frac{\partial \dot{x}_{2,k-1+j}}{\partial x_{2,k-2+j}} & \frac{\partial \dot{x}_{2,k-1+j}}{\partial t_{k-2+j}} \\ \frac{\partial x_{2,k-1+j}}{\partial \dot{x}_{1,k-2+j}} & \frac{\partial x_{2,k-1+j}}{\partial \dot{x}_{2,k-2+j}} & \frac{\partial x_{2,k-1+j}}{\partial x_{2,k-2+j}} & \frac{\partial x_{2,k-1+j}}{\partial t_{k-2+j}} \\ \frac{\partial t_{k-1+j}}{\partial \dot{x}_{1,k-2+j}} & \frac{\partial t_{k-1+j}}{\partial \dot{x}_{2,k-2+j}} & \frac{\partial t_{k-1+j}}{\partial x_{2,k-2+j}} & \frac{\partial t_{k-1+j}}{\partial t_{k-2+j}} \end{bmatrix}. \tag{35}$$

The entries of the matrices can be computed via implicit differentiation of (17)–(20), and their expressions are given in Appendix. For simplicity of computation here, we approximate the partial derivatives in (35) numerically, using a central difference approximation and small ($\approx 1e{-}4$) change in the variable of differentiation.

Fig. 4(c) shows the magnitude of the eigenvalues of $J_{P_2}J_{P_1}$ for the 1:1 symmetric solution. The four complex eigenvalues form 2 conjugate pairs for $A < 0.0172$. At $A \approx 0.0172$, one of the conjugate pairs becomes real, and the magnitude of one of the eigenvalues grows in magnitude with increasing A. Then $|\lambda| > 1$ for $A > 0.018$. This corresponds to the saddle node bifurcation point B_1, indicating the symmetry-breaking bifurcation as the symmetric 1:1 loses stability to the asymmetric 1:1 solution, consistent with Panels (a,b). Fig. 4(f) shows the magnitude of the eigenvalues of $J_{P_2}J_{P_1}$ for the 1:1 asymmetric solution for $0.020 < A < 0.0215$. The magnitude of the largest eigenvalue exceeds 1 (corresponding to $\lambda < -1$) at $A \approx 0.0205$, indicating a period doubling bifurcation labeled B_2, where the 1:1 solution loses stability to the $1{:}1/2T$ solution, consistent with Panels (d,e).

4.3. Other periodic solutions

The composition of maps to describe different periodic systems is not limited to 1:1 behavior. As above, we can derive a system of equations for other n: m periodic solutions, by combining the maps P_j from Section 3. We illustrate for a 2:1 periodic solution, following a similar procedure as above. We note that transitions from 1:1 to 2:1 solutions are typically associated with grazing bifurcations, in which an additional zero relative velocity impact is included in the 1:1 trajectory [28]. We do not demonstrate grazing here, as a full analysis would consider non-smooth bifurcations such as grazing, and their interplay with smooth bifurcations such as fold or period doubling. However, the construction of exact solutions and their stability analysis given here provides the foundation for future studies of both non-smooth and traditional (smooth) bifurcations in VI-NES-type frameworks.

The 2:1 behavior is captured by the composition $P_3 \circ P_2 \circ P_1$, indicating the sequence $L \to R \to L \to L$ over one forcing period T. Then we determine the state variables $\mathbf{s}_j$ for $j = k-1, k, k+1$, and $k+2$, with the periodic conditions

$$\begin{aligned} &P_3(P_2(P_1(\mathbf{s}_{k-1}))) = \mathbf{s}_{k+2} = \mathbf{s}_{k-1} \qquad t_{k+2} - t_{k-1} = T \\ &P_1(\mathbf{s}_{k-1}) = \mathbf{s}_k, \qquad P_2(\mathbf{s}_k) = \mathbf{s}_{k+1}\,, \end{aligned} \tag{36}$$

where, as above, equality for the t_{k+2} and t_{k-1} in $\mathbf{s}_{k+2} = \mathbf{s}_{k-1}$ is in the mod T sense, as indicated in (36). Then the system of equations to be solved follows the same structure as above. The state variables $\mathbf{s}_k$ and $\mathbf{s}_{k+1}$ on R and L are obtained using (25)–(29) to get $\mathbf{s}_k$, then calculating $\mathbf{s}_{k+1}$ using $\mathbf{s}_k$ on the right hand side of (30)–(31), with $x_{j,k+1}$ and $\dot{x}_{j,k+1}$ replacing $x_{j,k-1}$ and $\dot{x}_{j,k-1}$ in (29)–(31) for $j = 1, 2$. Then for the last pair of impacts on L corresponding to P_3, we have

$$\begin{aligned} x_{1,k-1} &= \mathcal{G}(t_{k+1}, t_{k+2}, x_{1,k+1}, \dot{x}_{1,k+1}, \dot{x}_{2,k+1}, \varphi) \\ \dot{x}_{1,k-1} &= \mathcal{H}(t_{k+1}, t_{k+2}, x_{1,k+1}, \dot{x}_{1,k+1}, \dot{x}_{2,k+1}, \varphi) \end{aligned} \tag{37}$$

$$\begin{aligned} x_{2,k-1} &= x_{2,k+1} + \left(\frac{1+r}{1+\mu}\dot{x}_{1,k+1} + \frac{\mu - r}{1+\mu}\dot{x}_{2,k+1} \right) \cdot (t_{k+1} - t_k) \\ \dot{x}_{2,k-1} &= \frac{1+r}{1+\mu}\dot{x}_{1,k+1} + \frac{\mu - r}{1+\mu}\dot{x}_{2,k+1} \end{aligned} \tag{38}$$

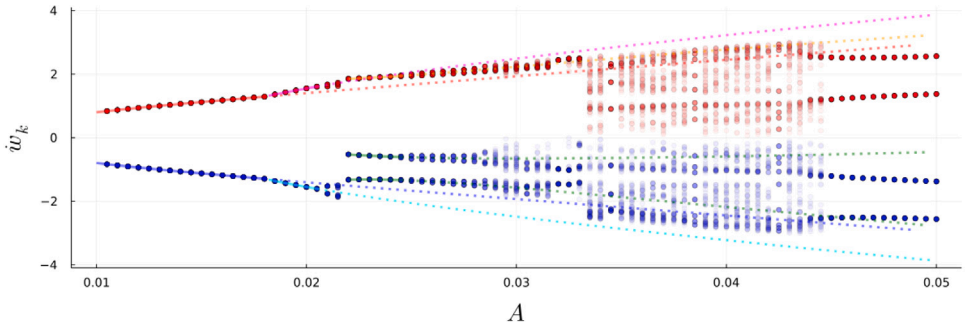

Fig. 5. Bifurcation diagram of $\dot{w}_k$ vs. A with $\mu = 0.01$, $\Omega = 1$, and $r = 0.65$, over a large range of A. Other parameters as in Table 1. Red and blue markers show the relative impact velocity on L and R, as obtained from numerical simulation. The individual markers are plotted with a low opacity, so that solid markers indicate regular repetition of those values, as in a stable periodic orbits, while light or blurry markers indicate irregular values, as in the chaotic behavior. The blue and red solid (dotted) lines show the stable (unstable) 1:1 symmetric solution obtained analytically. The magenta and cyan solid (dotted) lines show the stable (unstable) 1:1 asymmetric solution obtained analytically. The orange and green solid (dotted) lines show the stable (unstable) 2:1 solution obtained analytically. (For interpretation of the references to color in this figure legend, the reader is referred to the web version of this article.)

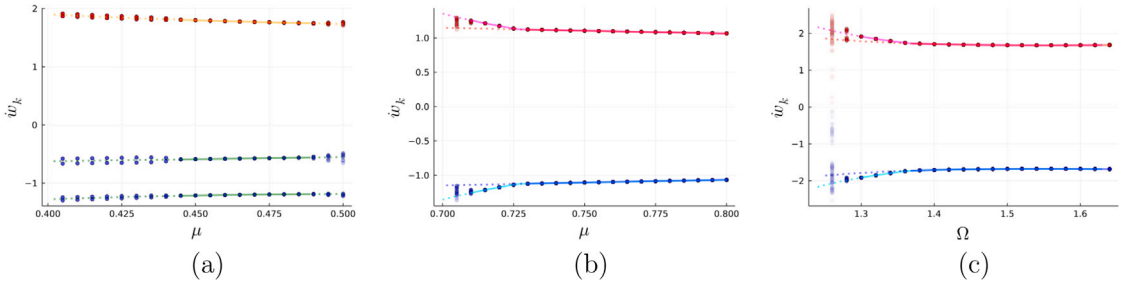

Fig. 6. Panels (a), (b): Bifurcation diagram of $\dot{w}_k$ vs. μ with $A = 0.5$, $\Omega = 1$; Panel (c): Bifurcation of $\dot{w}$ vs. Ω with $A = 0.8, \mu = 0.2$. In (a)–(c), red and blue dots show the relative impact velocity on L and R, respectively, as obtained from numerical simulation. In (b)–(c), red and blue (magenta and cyan) lines show symmetric (asymmetric) 1:1 solutions. In (a), orange and green lines show analytical 2:1 solutions. Solid (dotted) lines show stable (unstable) analytical solutions. (For interpretation of the references to color in this figure legend, the reader is referred to the web version of this article.)

$$x_{1,k-1} - x_{2,k-1} = -1 \qquad t_{k+2} = t_{k-1} + T\,. \tag{39}$$

Again, without loss of generality, we take $t_{k-1} = 0$ for a T periodic solution. Instead of (32) we determine three intervals between impacts Δt_j, $j = k-1, k, k+1$, such that $\Sigma_{j=k-1}^{k+1} \Delta t_j = T$.

Using the same approach to study the linear stability of the 2:1 periodic solution, we consider a fixed point $\mathbf{S}^* = (\mathbf{s}_1^*, \mathbf{s}_2^*, \mathbf{s}_3^*)$ for the corresponding composition $P_3 \circ P_2 \circ P_1$. Again we consider a corresponding periodic sequence $(\mathbf{s}_{k-1}, \mathbf{s}_k, \mathbf{s}_{k+1}, \mathbf{s}_{k+2}) = (\mathbf{s}_1^*, \mathbf{s}_2^*, \mathbf{s}_3^*, \mathbf{s}_1^*)$ and derive an equation for the perturbations to this sequence,

$$\begin{aligned} \mathbf{s}_{k+2} + \delta\mathbf{s}_{k+2} &= P_3(P_2(P_1(\mathbf{s}_{k-1} + \delta\mathbf{s}_{k-1}))) = P_3(P_2(P_1(\mathbf{s}_1^* + \delta\mathbf{s}_{k-1}))) \\ &\approx P_3(P_2(P_1(\mathbf{s}_1^*))) + J_{P_3}(\mathbf{s}_{k+1}) J_{P_2}(\mathbf{s}_k) J_{P_1}(\mathbf{s}_1^*) \delta\mathbf{s}_{k-1} \\ \implies \delta\mathbf{s}_{k+2} &\approx J_{P_3}(\mathbf{s}_3^*) J_{P_2}(\mathbf{s}_2^*) J_{P_1}(\mathbf{s}_1^*) \delta\mathbf{s}_{k-1}\,. \end{aligned} \tag{40}$$

Analogous to the linear stability analysis above, the eigenvalues of the matrix $J_{P_3} J_{P_2} J_{P_1}$ yield conditions for the linear stability of the 2:1 periodic solutions, with J_{P_j} taking the same form as in (35).

5. Comparison to numerical simulations

Above we have demonstrated how the analytical solution can be obtained for different periodic behaviors in the VI-NES model (8)–(9). Since the analysis is based on an exact solution via semi-analytical calculations, it can be applied over a range of parameters without any asymptotic limitations. The results also have implications for energy transfer, which we explore with a number of different measures.

5.1. Bifurcation scenarios for $\mu = O(1)$ and $|\Omega - 1| = O(1)$

In this section we compare the analytical and numerical results for 1:1 and 2:1 solutions over a range of parameters. Through this comparison we demonstrate a number of important results for this approach. First, we observe that this approach accurately provides

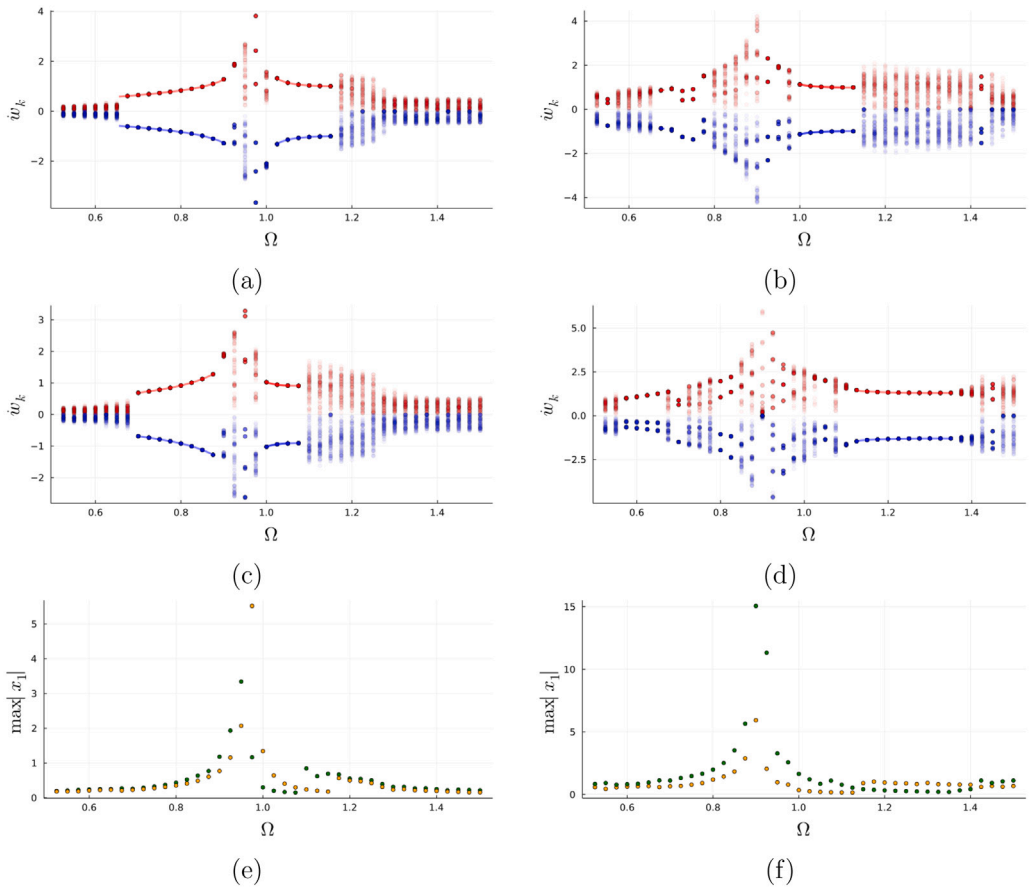

Fig. 7. Relative impact velocity on L (red) and R (blue) in (a)–(d) for (a) $\mu = 0.05, A = 0.1$; (b) $\mu = 0.2, A = 0.2$; (c) $\mu = 0.1, A = 0.1$; and (d) $\mu = 0.2, A = 0.4$. (e) $\max|x_1|$ for cases shown in (a) (orange dots) and (c) (green dots); (f) $\max|x_1|$ for cases shown in (b) (orange dots) and (d) (green dots);. (For interpretation of the references to color in this figure legend, the reader is referred to the web version of this article.)

the behavior over a large range of μ, A and ω, demonstrating that the analysis is not limited to asymptotic regimes considered previously, such as $\mu \ll 1$ or $\Omega \sim 1$. The good agreement indicates the advantage of our analysis for exploring different behaviors over a larger range of possible parameter values. Second, we see good agreement for different types of periodic solutions, and not only for 1:1 solutions. We also show agreement with stability results, from which we obtain information about transitions between different types of behavior. The advantage is that this analysis allows the study of a larger range of possible mechanisms for energy transfer.

In Fig. 5 we provide a "big picture" view of the bifurcation sequence for the relative impact velocity $\dot{w}_k$ as a function of external forcing A, in the case of $\mu \ll 1$ and $\Omega = 1$. There we compare the analytical results for 1:1 and 2:1 periodic solutions with the numerically obtained attracting behavior for smaller values of A. This comparison shows excellent agreement with the stable 1:1 and 2:1 behavior, and the analysis correctly predicts the loss of stability for these different behaviors, as is demonstrated by the change in line types. Additional sequences are shown for period doubling to apparently chaotic behavior and other periodic n:m solutions. We do not construct them here, but rather focus below on larger μ and variation in Ω.

Likewise, for these parameter combinations, a grazing bifurcation from a period doubled 1:1 period solution to a 2:1 periodic solution underlies the transition (for A just above 0.02), illustrated in Fig. 5. These types of transitions have been studied in detail for a vibro-impact energy harvester (VI-EH) in [28]. We do not pursue them here, given the complex sequences of smooth and non-smooth bifurcations that must all be considered for such transitions. For example, the grazing bifurcation in Fig. 5 occurs on a branch of unstable 1:1/pT solutions, and must be determined by following the unstable branch to the point where $\dot{w}_k = 0$, which is the definition of grazing. Based on the results of [28], the observed transition between 1:1/$2T$ and 2:1 periodic solutions likely occurs via a fold bifurcation that connects stable and unstable 2:1 solutions.

Fig. 6 provides a comparison of the analytical and stability results for 1:1 and 2:1 periodic solutions in cases where the small mass m is a larger percentage of M, ranging over 40%–80%. Clearly this is not in the range of light absorption, but nevertheless demonstrates the flexibility of the approach to consider a wide variety of scenarios for energy transfer. We also consider scenarios where $\Omega > 1$, with larger external forcing (larger A) in all cases. Once again we see good agreement between the attracting 1:1 and

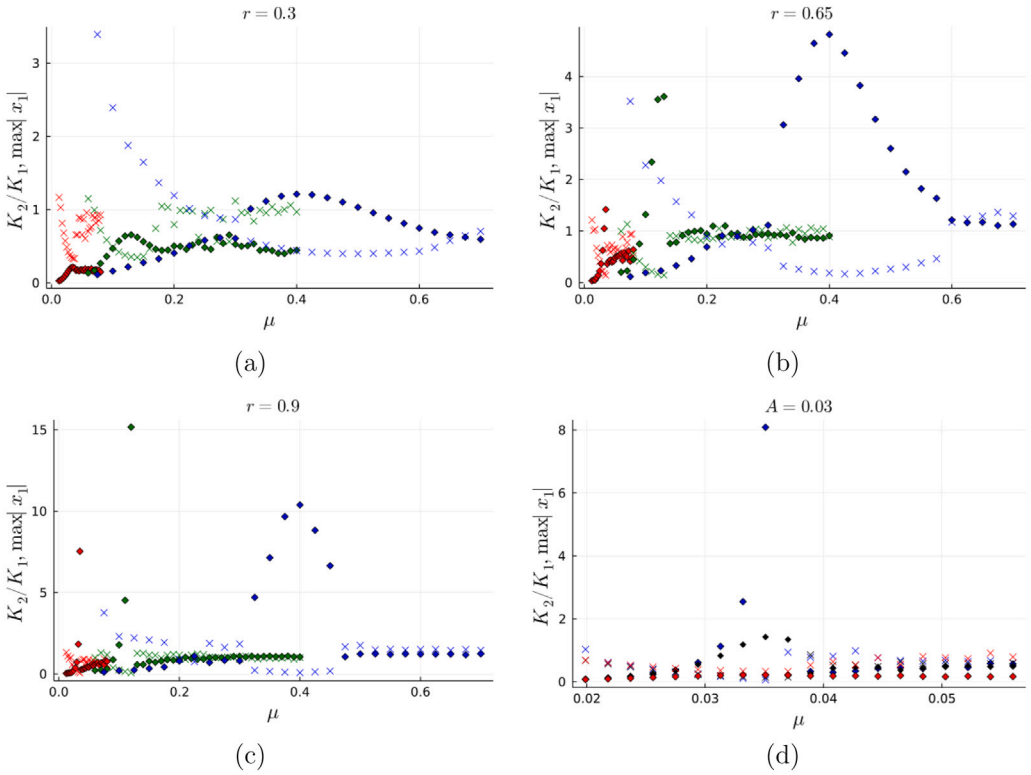

Fig. 8. Panels (a)–(c): K_2/K_1 (diamonds) and $\max|x_1|$ (×) vs. μ for three different values of A: $A = .03$ (red), $A = .1$ (green), $A = .3$ (blue), and three different values of r as indicated. Panel (d) provides a zoom-in view for $A = .03$ as in (a)–(c) for $r = 0.3$ (red), $r = 0.65$ (black), and for $r = 0.9$ (blue). For all plots $\Omega = 1$. (For interpretation of the references to color in this figure legend, the reader is referred to the web version of this article.)

2:1 solutions, as well as the stability analysis capturing symmetry breaking bifurcations and period doubling bifurcations. These results indicate that the 1:1 or other regular periodic solutions are not limited to regions near $\Omega = 1$, but rather are observed for other values of Ω, where the ratio of the forcing frequency to natural frequency is away from unity. In these scenarios it is necessary to analyze a range of forcing frequencies away from the natural frequency, for identifying the best options for increased energy transfer.

Fig. 7 shows $\dot{w}_k$ vs. a range of Ω, for different combinations of μ and A. These figures illustrate different regions where periodic and chaotic behaviors occur; for example, for larger A, the 1:1 periodic behavior is shifted to larger values of $\Omega > 1$, as shown in Panel (d). Likewise for smaller values of A there are 1:1 solutions that extend for $\Omega < 1$, as in Panels (a)–(b). There also appear to be more complex, yet periodic behaviors that occur near $\Omega = 1$; while we do not analyze them here, they are potential candidates for the map-based analysis used above. The graphs of $\max|x_1|$ in Panels (e)–(f) illustrate that the 1:1 behavior tends to reduce this particular energy measure. Comparing these graphs with the corresponding bifurcation plots above them, we observe that, for certain parameter combinations, other types of behavior can yield similar results for $\max|x_1|$ as that observed for 1:1 behavior.

6. Energy measures

In Figs. 8 and 9 we show results for the energy measures $\max|x_1|$ and the ratio of the kinetic energies of the small to the large mass, K_2/K_1 (11). These measures are shown for different values of $\mu = m/M$, A and Ω. While we leave for future study a comprehensive study of the energy transfer for different types of periodic behavior, these examples illustrate both the influence of different types of periodic solutions on energy transfer and the large parameter ranges over which those differences can be observed. Thus, the analytical results for the appearance and stability of these different behaviors can provide a more complete picture of options for efficient energy transfer.

The graphs illustrate parameter ranges with desirable behavior in energy transfer, that is, larger K_2/K_1 and small $\max|x_1|$, in contrast to other regions where K_2/K_1 is small and/or $\max|x_1|$ is larger. These regions are of course dependent on the forcing amplitude A, and the relative size of μ, as well as on Ω. The response also depends on r, with the variation increasing with r, as observed from the ranges on the vertical axes.

Fig. 8 illustrates how these measures change with μ for fixed A and Ω. While increasing μ tends to limit $\max|x_1|$, K_2/K_1, does not increase monotonically with μ, instead showing pronounced peaks at certain values. This is due to the change in underlying behavior that may or may not promote large K_2/K_1. The location of the peak depends on the relative size of A and μ, which can

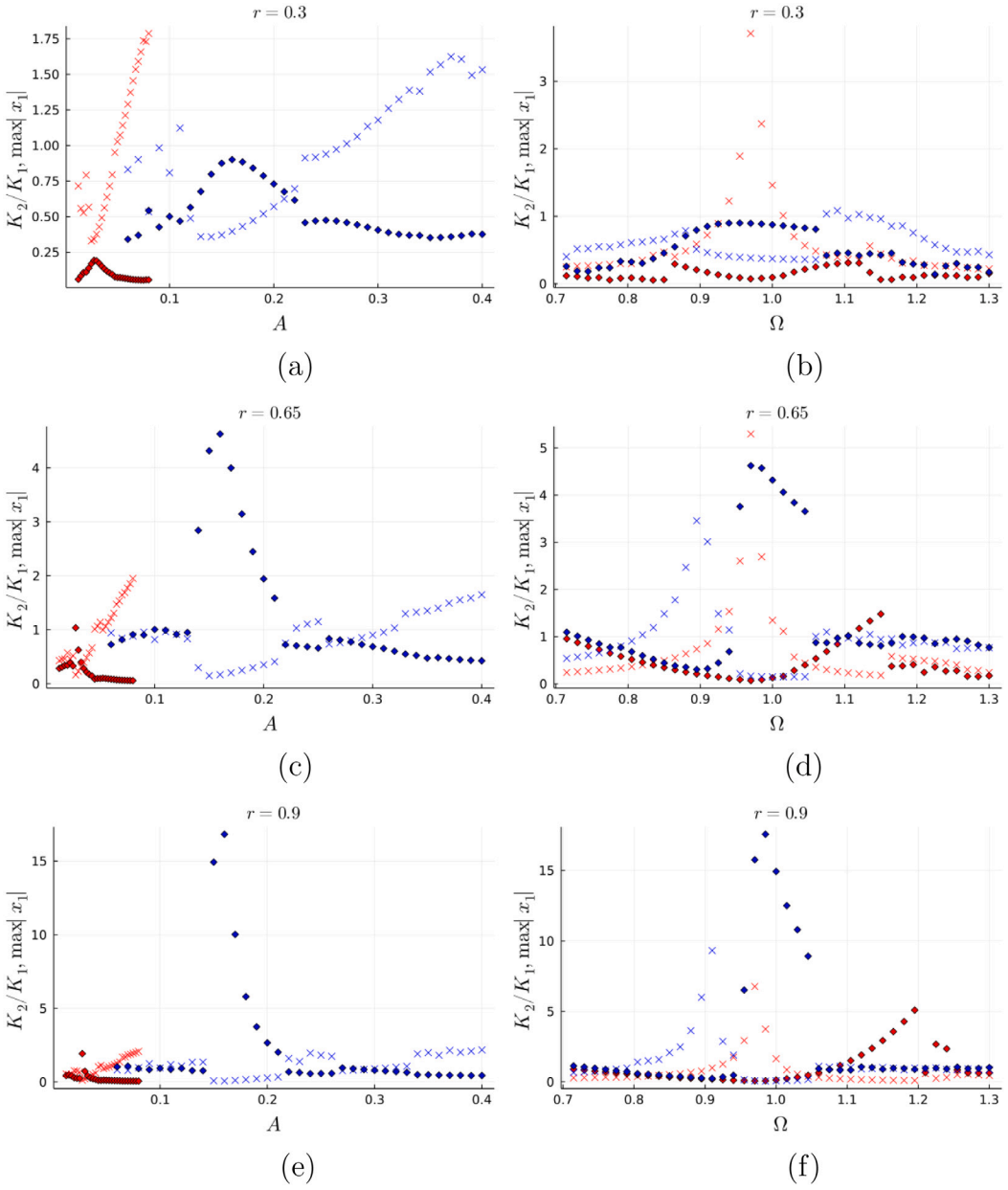

Fig. 9. K_2/K_1 (diamonds) and $\max|x_1|$ (×) for different parameter combinations, with $r = 0.3$, $r = 0.65$, $r = 0.9$ and $\Omega = 1$. Left column: Energy measures vs. A for different values of μ: $\mu = .03$ (red), $\mu = .2$ (blue). Right column: Energy measures vs. Ω for two different combinations of μ and A: $\mu = .05$, $A = .1$ (red), $\mu = .2$, $A = .15$ (blue). (For interpretation of the references to color in this figure legend, the reader is referred to the web version of this article.)

be observed, for example, for $r = 0.65$ in Fig. 8(b); i.e., peaks in K_2/K_1 corresponding to smaller A values, appear at smaller μ values (see also Fig. 8(d) for zoom-ins on smaller μ.). Both Figs. 8 and 9 (left column) confirm that small values of μ do not provide effective TET at relatively large excitation amplitudes A; rather for larger A, a larger μ is needed. Changing r influences the height of the peaks without shifting their locations.

Fig. 9 (right column) demonstrates that the optimal TET does not necessarily occur near $\Omega = 1$, depending on the values of A and μ. This follows from the fact that the optimal periodic 1:1 behavior may occur for other values of Ω, as observed in Fig. 7, and discussed further in the context of that figure. For smaller values of r, $\max|x_1|$ has a peak for the values $\mu = 0.05$, $A = 0.1$ (red crosses), with limited K_2/K_1, whereas for larger values of μ and A the energy transfer is more efficient (larger K_2/K_1, smaller $\max|x_1|$). At the same time, on an absolute scale, for the larger r values the energy dissipation due to impact (shown by red crosses) has been reduced while the peak of K_2/K_1 increases.

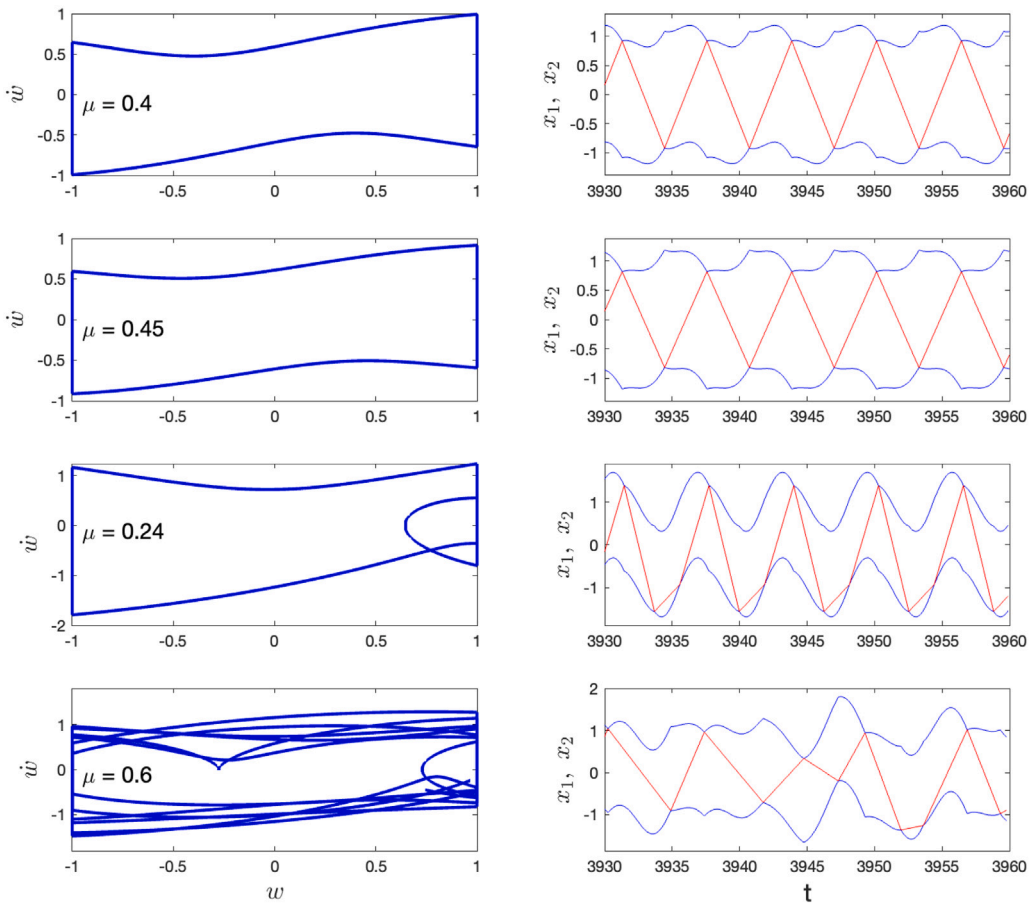

Fig. 10. Phase planes (left column) for relative displacement w and velocity $\dot{w}$ and corresponding time series (right column) for $x_1 \pm b$ (blue) and x_2 (red) illustrating behavior for different energy levels as shown in Fig. 8(b) for $r = 0.65$. Results shown for $A = 0.3$ and $\Omega = 1$, with the 1:1 behavior at the peak of K_2/K_1 shown in (a) $\mu = 0.4$, and other 1:1 behavior for (b) $\mu = 0.45$, with smaller K_2/K_1. Behavior for even smaller K_2/K_1 include 2:1 solutions at (c) $\mu = 0.24$, and (d) complex dynamics at $\mu = 0.6$. (For interpretation of the references to color in this figure legend, the reader is referred to the web version of this article.)

Fig. 10 shows the time series and phase planes for different values of μ with $A = 0.3$, $r = 0.65$, and $\Omega = 1$, illustrating the different solutions corresponding to the different energy transfer measures shown in Fig. 8(b). The four rows show four different behaviors, including at and nearby the value of μ yielding the K_2/K_1 peak in Fig. 8(b) for $A = 0.3$. Fig. 10(a) shows the periodic 1:1 solution at which there is a maximum in K_2/K_1 and the corresponding minimum of $\max|x_1|$, as achieved at $\mu \approx 0.4$. In that case the impact phase is optimal, with impacts near the peaks of the oscillation of the LO, as the ball is moving in the opposite direction, yielding larger relative impact velocities. Panel (b) shows another 1:1 solution for slightly larger μ, for which the impact occurs at the peak of oscillation of the LO, yielding an impact phase with reduced efficiency. There the LO has slowed down, thus yielding a smaller relative impact velocity when impacting the ball. We contrast this behavior with the 2:1 behavior shown in Panel (c) for smaller μ, where, for each cycle, the first impact on the left of the cavity occurs when the ball and LO are moving in the same direction, followed by a second impact on the left with low relative impact velocity. For the 2:1 behavior, both types of energy measures are limited, which may be beneficial when trying to control $|x_1|$. Panel (d) shows another complex behavior for larger μ, which has similar energy measure levels as the 2:1 behavior. Thus these example illustrate that not only the type of periodic solution but also its impact phase are important features contributing to efficient energy transfer.

For Fig. 11, the top and bottom rows correspond to the same parameter values, but different energy transfer as shown in Fig. 9(d) for $\Omega \approx 1.17$, $A = 0.1$, $\mu = 0.05$. Following the branch of red diamonds (K_2/K_1) for Ω increasing up to $\Omega \approx 1.17$, we trace a branch of 1:1 solutions with larger K_2/K_1, whose dynamics are illustrated in the top row of Fig. 11. In contrast, following the solutions corresponding to Ω decreasing down to $\Omega \approx 1.17$, we trace chaotic solutions as shown in the bottom row of Fig. 11, with a lower K_2/K_1 (larger $\max|x_1|$) in Fig. 9(d) as compared to that of the 1:1 solution. Then these two simulations illustrate bi-stability for these two types of solutions, each dependent on specific initial conditions. The examples shown in Figs. 10–11 illustrate that different types of periodic solutions yield a range of options for energy transfer, motivating future investigation that relies on analytical results. For example, optimizing impact phase and operating near parameter regions with bi-stability requires a careful understanding of the dynamical behavior, in order to achieve efficient energy transfer.

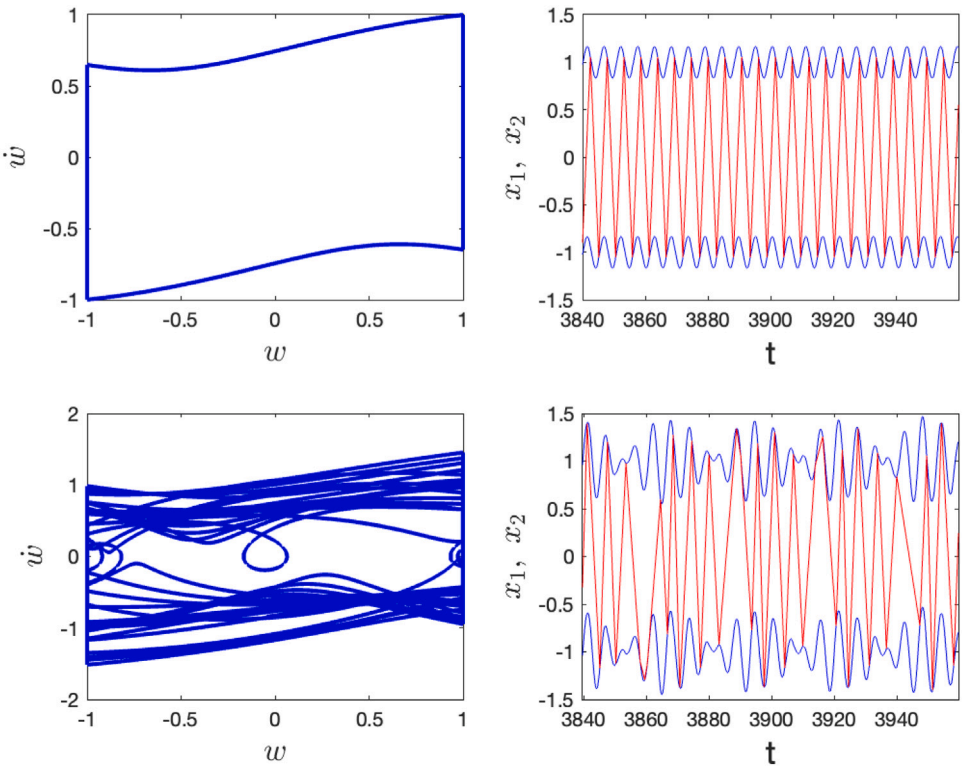

Fig. 11. Phase planes (left column) for relative displacement w and velocity $\dot{w}$ and corresponding time series (right column) for $x_1 \pm b$ (blue) and x_2 (red) illustrating behavior for different energy levels as shown in Fig. 9(b) for $r = 0.65$, $A = .1$, $\mu = .05$, and $\Omega \approx 1.17$. The top row shows 1:1 behavior, with initial condition at a stable 1:1 behavior for $\Omega < 1.17$ (larger K_2/K_1); in contrast, the bottom row shows complex behavior, with initial condition at chaotic behavior for $\Omega > 1.17$ (lower K_2/K_1). These two results illustrate bi-stability of two different behaviors, with different energy transfer properties. (For interpretation of the references to color in this figure legend, the reader is referred to the web version of this article.)

7. Conclusion and future directions

We consider a model of a vibro-impact nonlinear energy sink (VI-NES), where energy transfer from an externally forced main mass to a small mass is achieved via impacts. A ball, the smaller mass, moves within a cavity of the larger mass, with the impacts on either end of the cavity potentially limiting the oscillations of the larger system. While a simple periodic behavior, with two alternating impacts on either end of the cavity occurring during one forcing period, has been observed as an efficient behavior for this energy transfer, a systematic treatment of the full range of parameters is required in order to understand and predict the beneficial states across all possible scenarios. Starting with a map-based approach, recently used for an inclined impact pair model without energy transfer from the main mass to ball, we develop a new approach for the setting where there is such energy transfer. This approach allows us to capture the exact dynamics of the VI-NES system without restricting the range of parameters, in contrast to other recent work in which an approximate reduced model is valid only for small mass of the ball, small amplitude, and a limited forcing frequency range. The map-based approach yields analytical results for different types of periodic solutions for all ratios of the two masses, forcing amplitudes, and ratios of forcing frequencies to the natural frequency of the main mass. Since the maps are applicable for any combination of impact sequences, the construction allows a flexible consideration of different types of periodic solutions with any possible impact sequences in the full two DoF model of VI-NES. The analytical results provide the physically important characteristics of these solutions, including the impact phase and the relatively impact velocities.

The map-based construction is the basis for the bifurcation analysis for the full VI-NES system, providing both exact solutions and linear stability analyses for the various possible periodic dynamics. For example, here we provide results for 1:1 and 2:1 periodic solutions, indicating parametric conditions that lead to grazing bifurcations with zero relative impact velocity. The results then motivate future studies that explore the interplay of non-smooth (such as grazing) and classical (such as period doubling and fold) bifurcations, together with their observability and implications. The analytical treatment above mirrors that in [32] for the relative dynamics of a vibro-impact energy harvester (VI-EH). Furthermore, the recent study [28] of the complex interplay of bifurcations for the general impact pair provides a road-map for understanding sequences of different bifurcations within VI-NES. As shown in this paper, in the VI-NES context the analysis must be generalized to handle the maps in terms of the absolute dynamics of both the small and large masses. Treating this larger system is necessary for capturing the feedback between the masses at impact. The method does not depend on limitations on the parameter ranges, as demonstrated by the excellent agreement between the analytical results for

different periodic solutions and numerical simulations over parameter ranges with $O(1)$ mass of the ball, forcing frequencies that are not the same as the natural frequency, and large amplitude forcing. Preliminary calculations also point to routes to (near)-sticking behavior for combinations of larger forcing amplitude and larger mass. The analysis presented here can predict the sequences of bifurcations to n:1 behavior, where the impact phase and frequency ratio $\Omega \neq 1$ play important roles in the energy transfer.

While not the main focus of this study, a variety of examples are provided that show how different periodic behavior influences two energy measures, the maximum amplitude of the main mass oscillations, and the ratio of average kinetic energies of the two masses. These examples highlight the significance of different types of periodic behavior in energy transfer, which depend on key features such as the impact phase, sequence and number of impacts per forcing period, and stability and bi-stability of competing behaviors. The examples also illustrate scenarios where the desirability of different combinations of parameters may vary with the primary goal of energy transfer, e.g. limiting the oscillations of the main mass, increasing the transfer between the masses, or other priorities that may be captured by other energy measures.

Regardless of the primary goal, the necessary features are directly obtained from analytical results, which then can be used to identify optimal parameter settings. The analytical approach is a foundation for a future systematic study of the energy transfer efficiency of a variety of behaviors in the VI-NES system. The results here provide the opportunity to compare experiments with analytical predictions for optimal design over parameter ranges outside of those studied in the asymptotic regime focused on $\mu \ll 1$, $\Omega \approx 1$ and small forcing amplitude, as in e.g. [17,22] and other previous work. An experimental rig is being developed at ISVR, University of Southampton, to conduct the experiments and their results will be reported in our next publication.

Other future directions include integration of the exact approach of this paper to study systems with combined VI-NES and classical NES, motivated by recent studies that seek to combine the advantages of both. For example, this is particularly attractive in considering different configurations, such as using VI-NES and classical NES in parallel, for which the numerical simulations in [25] show substantial reduction in displacement of the LO as compared with classical NES or VI-NES alone. In contrast, [26,27] both choose a different design, a classical cubic NES within bilateral barriers. The impacts yield opportunities for additional broadband TET efficiency, given an appropriate range of barrier gap size. As with previous multiple scale approaches, the analyses based on slow modulations in [25,26], and [27] are limited in parameter range and types of phenomena. Furthermore [27] shows that 2:1-type solutions can also occur for the cubic NES with barrier impacts, also noting that previous slow modulation asymptotic approaches cannot capture this behavior. In addition, we expect that the development of a novel global stability analysis, on-going work in the general impact pair and VI-EH settings, will be valuable for future study of VI-NES in stochastic settings.

Data availability

Data will be made available on request.

Acknowledgments

The authors gratefully acknowledge partial funding for this work from NSF-CMMI, USA 2009270 and EPSRC, UK EP/V034391/1.

Declaration of competing interest

The authors declare that they have no known competing financial interests or personal relationships that could have appeared to influence the work reported in this paper.

Appendix. The Jacobian matrix

Complementary to the semi-analytical approximation to the Jacobian matrices in Section 4.2, they can be obtained analytically using implicit differentiation. Considering (25)–(28), we demonstrate the steps in this process for the entries $\frac{\partial \dot{y}_{j,k}}{\partial z_{k-1}}$, for $y, z = \dot{x}_1, x_2, \dot{x}_2, t$.

From (28), we obtain immediately

$$\frac{\partial \dot{x}_{2,k}}{\partial \dot{x}_{2,k-1}} = \frac{\mu - r}{1+\mu} \qquad \frac{\partial \dot{x}_{2,k}}{\partial \dot{x}_{1,k-1}} = \frac{1+r}{1+\mu} \qquad \frac{\partial \dot{x}_{2,k}}{\partial x_{2,k-1}} = \frac{\partial \dot{x}_{2,k}}{\partial t_{k-1}} = 0\,. \tag{A.1}$$

From (25) and (27) we obtain coupled equations for the derivatives of t_k and $x_{2,k-1}$ in (35). First, from (27)

$$\begin{aligned}
\frac{\partial x_{2,k}}{\partial t_{k-1}} &= \mathcal{R}(\dot{x}_{1,k-1}, \dot{x}_{2,k-1})\Big(\frac{\partial t_k}{\partial t_{k-1}} - 1\Big), \\
\frac{\partial x_{2,k}}{\partial \dot{x}_{1,k-1}} &= \frac{1+r}{1+\mu}(t_k - t_{k-1}) + \frac{\partial t_k}{\partial \dot{x}_{1,k-1}}\mathcal{R}(\dot{x}_{1,k-1}, \dot{x}_{2,k-1}) \\
\frac{\partial x_{2,k}}{\partial \dot{x}_{2,k-1}} &= \frac{\mu - r}{1+\mu}(t_k - t_{k-1}) + \frac{\partial t_k}{\partial \dot{x}_{2,k-1}}\mathcal{R}(\dot{x}_{1,k-1}, \dot{x}_{2,k-1}) \\
\frac{\partial x_{2,k}}{\partial x_{2,k-1}} &= 1 + \frac{\partial t_k}{\partial \dot{x}_{2,k-1}}\mathcal{R}(\dot{x}_{1,k-1}, \dot{x}_{2,k-1}), \qquad \mathcal{R}(\dot{x}_{1,k-1}, \dot{x}_{2,k-1}) = \Big(\frac{1+r}{1+\mu}\dot{x}_{1,k-1} + \frac{\mu - r}{1+\mu}\dot{x}_{2,k-1}\Big)\,.
\end{aligned} \tag{A.2}$$

Then from (25), using $x_{1,k} = x_{2,k} \pm 1$ we have

$$\frac{\partial x_{2,k}}{\partial z_{k-1}} = \frac{\partial t_k}{\partial z_{k-1}} h(t_k) + e^{-\lambda t_k/2}\sin(\gamma t_k)\frac{\partial a_1}{\partial z_{k-1}} + e^{-\lambda t_k/2}\cos(\gamma t_k)\frac{\partial a_2}{\partial z_{k-1}}, \tag{A.3}$$

for z_{k-1} replaced by $t_{k-1}, x_{2,k-1}, \dot{x}_{2,k-1}, \dot{x}_{1,k-1}$ and

$$\begin{aligned} h(t_k) &= e^{-\lambda t_k/2}\frac{2\gamma a_1 - \lambda a_2}{2}\cos(\gamma t_k) \\ &- e^{-\lambda t_k/2}\frac{\lambda a_1 + 2\gamma a_2}{2}\sin(\gamma t_k) + b_1\Omega\cos(\Omega t_k + \varphi) - b_2\Omega\sin(\Omega t_k + \varphi). \end{aligned} \tag{A.4}$$

From (25) and (26) we obtain coupled equations for the derivatives of t_k and $\dot{x}_{1,k}$ in (35). From (26) we have

$$\begin{aligned} \frac{\partial \dot{x}_{1,k}}{\partial t_{k-1}} &= \frac{\partial t_k}{\partial t_{k-1}} j_3(t_k) + \frac{\partial a_1}{\partial t_{k-1}} j_1(t_k) + \frac{\partial a_2}{\partial t_{k-1}} j_2(t_k) \\ \frac{\partial \dot{x}_{1,k}}{\partial x_{2,k-1}} &= \frac{\partial t_k}{\partial x_{2,k-1}} j_3(t_k) + \frac{\partial a_1}{\partial x_{2,k-1}} j_1(t_k) + \frac{\partial a_2}{\partial x_{2,k-1}} j_2(t_k) \\ \frac{\partial \dot{x}_{1,k}}{\partial \dot{x}_{2,k-1}} &= \frac{\partial t_k}{\partial \dot{x}_{2,k-1}} j_3(t_k) + \frac{\partial a_1}{\partial \dot{x}_{2,k-1}} j_1(t_k) + \frac{\partial a_2}{\partial \dot{x}_{2,k-1}} j_2(t_k) \\ \frac{\partial \dot{x}_{1,k}}{\partial \dot{x}_{1,k-1}} &= \frac{\partial t_k}{\partial \dot{x}_{1,k-1}} j_3(t_k) + \frac{\partial a_1}{\partial \dot{x}_{1,k-1}} j_1(t_k) + \frac{\partial a_2}{\partial \dot{x}_{1,k-1}} j_2(t_k), \end{aligned} \tag{A.5}$$

and

$$\begin{aligned} j_1(t_k) &= \frac{-\lambda}{2}e^{-\lambda t_k/2}\sin(\gamma t_k) + \gamma e^{-\lambda t_k/2}\cos(\gamma t_k) \\ j_2(t_k) &= \frac{-\lambda}{2}e^{-\lambda t_k/2}\cos(\gamma t_k) - \gamma e^{-\lambda t_k/2}\sin(\gamma t_k) \\ j_3(t_k) &= \frac{a_1\lambda^2 - 4a_1\gamma^2 + 4a_2\lambda\gamma}{4}e^{-\lambda t_k/2}\sin(\gamma t_k) + \frac{2a_1\gamma\lambda - 2a_1\lambda\gamma + a_2\lambda^2 - 4a_2\gamma^2}{4}e^{-\lambda t_k/2}\cos(\gamma t_k) \\ &- b_1\Omega^2\sin(\Omega t_k + \varphi) - b_2\Omega^2\cos(\Omega t_k + \varphi). \end{aligned} \tag{A.6}$$

From (21) we give simplified expressions for $a_{1,k-1}$ and $a_{2,k-1}$, and drop the subscript $k-1$ for the remainder of these calculations

$$\begin{aligned} a_1 = \frac{e^{\lambda t_{k-1}}}{-\gamma}\Big([\frac{-\lambda}{2}\cos(\gamma t_{k-1}) - \gamma\sin(\gamma t_{k-1})][x_{1,k-1} - b_1\sin(\Omega t_{k-1} + \varphi) + b_2\cos(\Omega t_{k-1} + \varphi)] - \\ \cos(\gamma t_{k-1})[\frac{1 - r\mu}{1 + \mu}\dot{x}_{1,k-1} + \frac{r\mu + \mu}{1 + \mu}\dot{x}_{2,k-1} - b_1\Omega\cos(\Omega t_{k-1} + \varphi) - b_2\Omega\sin(\Omega t_{k-1} + \varphi)]\Big) \end{aligned} \tag{A.7}$$

$$\begin{aligned} a_2 = \frac{e^{\lambda t_{k-1}}}{-\gamma}\Big([\frac{\lambda}{2}\sin(\gamma t_{k-1}) - \gamma\cos(\gamma t_{k-1})][x_{1,k-1} - b_1\sin(\Omega t_{k-1} + \varphi) + b_2\cos(\Omega t_{k-1} + \varphi)] + \\ \sin(\gamma t_{k-1})[\frac{1 - r\mu}{1 + \mu}\dot{x}_{1,k-1} + \frac{r\mu + \mu}{1 + \mu}\dot{x}_{2,k-1} - b_1\Omega\cos(\Omega t_{k-1} + \varphi) - b_2\Omega\sin(\Omega t_{k-1} + \varphi)]\Big). \end{aligned} \tag{A.8}$$

We differentiate $a_{1,k-1}$ and $a_{2,k-1}$ with respect to $\dot{x}_{1,k-1}$ $\dot{x}_{2,k-1}$, $x_{2,k-1}$

$$\begin{aligned} \frac{\partial a_1}{\partial \dot{x}_{1,k-1}} &= \frac{e^{\lambda t_{k-1}}}{\gamma}\cdot\frac{1 - r\mu}{1 + \mu}(\cos(\gamma t_{k-1})) \qquad \frac{\partial a_2}{\partial \dot{x}_{1,k-1}} = \frac{e^{\lambda t_{k-1}}}{-\gamma}\cdot\frac{1 - r\mu}{1 + \mu}(\sin(\gamma t_{k-1})) \\ \frac{\partial a_1}{\partial \dot{x}_{2,k-1}} &= \frac{e^{\lambda t_{k-1}}}{\gamma}\cdot\frac{r\mu + \mu}{1 + \mu}(\cos(\gamma t_{k-1})) \qquad \frac{\partial a_2}{\partial \dot{x}_{2,k-1}} = \frac{e^{\lambda t_{k-1}}}{-\gamma}\cdot\frac{r\mu + \mu}{1 + \mu}(\sin(\gamma t_{k-1})) \\ \frac{\partial a_1}{\partial x_{2,k-1}} &= e^{\lambda t_{k-1}}[\sin(\gamma t_{k-1}) + \frac{\lambda}{2\gamma}\cos(\gamma t_{k-1})] \qquad \frac{\partial a_2}{\partial x_{2,k-1}} = e^{\lambda t_{k-1}}[\cos(\gamma t_{k-1}) - \frac{\lambda}{2\gamma}\cos(\gamma t_{k-1})], \end{aligned} \tag{A.9}$$

and also with respect to t_{k-1},

$$\begin{aligned} \frac{\partial a_1}{\partial t_{k-1}} &= \lambda a_1 + \frac{e^{\lambda t_{k-1}}}{-\gamma}\Big([\frac{-\lambda}{2}\cos(\gamma t_{k-1}) - \gamma\sin(\gamma t_{k-1})]\cdot \\ &\quad [\frac{\partial x_{1,k-1}}{\partial t_{k-1}} - b_1\Omega\cos(\Omega t_{k-1} + \varphi) - b_2\Omega\sin(\Omega t_{k-1} + \varphi)] \\ &+ [\frac{\lambda\gamma}{2}\sin(\gamma t_{k-1}) - \gamma^2\cos(\gamma t_{k-1})][x_{1,k-1} - b_1\sin(\Omega t_{k-1} + \varphi) + b_2\cos(\Omega t_{k-1} + \varphi)] \\ &+ \gamma\sin(\gamma t_{k-1})[\frac{1 - r\mu}{1 + \mu}\dot{x}_{1,k-1} + \frac{r\mu + \mu}{1 + \mu}\dot{x}_{2,k-1} - b_1\Omega\cos(\Omega t_{k-1} + \varphi) - b_2\Omega\sin(\Omega t_{k-1} + \varphi)] \\ &- \cos(\gamma t_{k-1})[b_1\Omega^2\sin(\Omega t_{k-1} + \varphi) - b_2\Omega^2\cos(\Omega t_{k-1} + \varphi)]\Big) \\ \frac{\partial a_2}{\partial t_{k-1}} &= \lambda a_2 + \frac{e^{\lambda t_{k-1}}}{-\gamma}\Big([\frac{-\lambda}{2}\cos(\gamma t_{k-1}) - \gamma\sin(\gamma t_{k-1})]\cdot \\ &\quad [\frac{\partial x_{1,k-1}}{\partial t_{k-1}} - b_1\Omega\cos(\Omega t_{k-1} + \varphi) - b_2\Omega\sin(\Omega t_{k-1} + \varphi)] \end{aligned}$$

$$+\ [\frac{\lambda\gamma}{2}\sin(\gamma t_{k-1}) - \gamma^2\cos(\gamma t_{k-1})][x_{1,k-1} - b_1\sin(\Omega t_{k-1}+\varphi) + b_2\cos(\Omega t_{k-1}+\varphi)]$$
$$+\ \gamma\sin(\gamma t_{k-1})[\frac{1-r\mu}{1+\mu}\dot{x}_{1,k-1} + \frac{r\mu+\mu}{1+\mu}\dot{x}_{2,k-1} - b_1\Omega\cos(\Omega t_{k-1}+\varphi) - b_2\Omega\sin(\Omega t_{k-1}+\varphi)]$$
$$-\ \cos(\gamma t_{k-1})[b_1\Omega^2\sin(\Omega t_{k-1}+\varphi) - b_2\Omega^2\cos(\Omega t_{k-1}+\varphi)]\ \Big)\ . \tag{A.10}$$

References

[1] A.F. Vakakis, O.V. Gendelman, L.A. Bergman, D.M. McFarland, G. G. Kerschen, Y.S. Lee, Nonlinear Targeted Energy Transfer in Mechanical and Structural Systems, in: Solid Mechanics and Its Applications (SMIA), vol. 156, Springer, 2009.

[2] Ivan Yegorov (Egorov), Austin Uden, Daniil Yurchenko, Optimal performance comparison of nonlinear energy sinks and linear tuned mass dampers, in: International Design Engineering Technical Conferences and Computers and Information in Engineering Conference, in: vol. 9: 17th International Conference on Multibody Systems, Nonlinear Dynamics, and Control (MSNDC), 2021.

[3] G. Kerschen, M. Peeters, J.-C. Golinval, A.F. Vakakis, Nonlinear normal modes, part I: A useful framework for the structural dynamicist, Mech. Syst. Signal Process. 23 (2009) 170–194.

[4] Y. Lee, A.F. Vakakis, L. Bergman, D. D. McFarland, G. Kerschen, F. Nucera, S. Tsakirtzis, P. Panagopoulos, Passive non-linear targeted energy transfer and its applications to vibration absorption: A review, Proc. Inst. Mech. Eng. Part K (222) (2008) 77–134.

[5] Alexander F. Vakakis, Oleg V. Gendelman, Lawrence A. Bergman, Alireza Mojahed, Majdi Gzal, Nonlinear targeted energy transfer: State of the art and new perspectives, Nonlinear Dynam. 108 (2022) 711–741.

[6] Haiqin Li, Ang Li, Xianren Kong, Huai Xiong, Dynamics of an electromagnetic vibro-impact nonlinear energy sink, applications in energy harvesting and vibration absorption, Nonlinear Dynam. 108 (2022) 1807–1819.

[7] Tianming Huang, D. Michael McFarland, Alexander F. Vakakis, Oleg V. Gendelman, Lawrence A. Bergman, Huancai Lu, Energy transmission by impact in a system of two discrete oscillators, Nonlinear Dynam. 100 (2020) 135–145.

[8] A. Afsharfard, Suppressing forced vibrations of structures using smart vibro-impact systems, Nonlinear Dynam. 83 (3) (2016) 1643–1652.

[9] P. Lieber, D.P. Jensen, An acceleration damper: Development, design and some applications, Trans. ASME 67 (10) (1945) 523–530.

[10] Raouf A. Ibrahim, Vibro-impact dynamics: Modeling, mapping and applications, in: Lecture Notes in Applied and Computational Mechanics, 2009.

[11] L. Gagnon, M. Morandini, G.L. Ghiringhelli, A review of particle damping modeling and testing, J. Sound Vib. 459 (2019) 114865.

[12] O.V. Gendelman, A. Alloni, Dynamics of forced system with vibro-impact energy sink, J. Sound Vib. 358 (2015) 301–314.

[13] Tao Li, Sebastien Seguy, Alain Berlioz, Optimization mechanism of targeted energy transfer with vibro-impact energy sink under periodic and transient excitation, Nonlinear Dynam. 87 (2016) 2415–2433.

[14] Balkis Youssef, Remco Leine, A complete set of design rules for a vibro-impact NES based on a multiple scales approximation of a nonlinear mode, J. Sound Vib. 501 (2021) 116043.

[15] I. Karayannis, A.F. Vakakis, F. Georgiades, Vibro-impact attachments as shock absorbers, Proc. Inst. Mech. Eng. C: J. Mech. Eng. Sci. 222 (2008) 1899–1908.

[16] T. Li, D. Qiu, S. Seguy, A. Berlioz, Activation characteristic of a vibro-impact energy sink and its application to chatter control in turning, J. Sound Vib. 405 (2017) 1–18.

[17] D. Qiu, S. Seguy, M. Paredes, Design criteria for optimally tuned vibro-impact nonlinear energy sink, J. Sound Vib. (442) (2019) 497–513.

[18] Haiqin Li, Ang Li, Potential of a vibro-impact nonlinear energy sink for energy harvesting, Mech. Syst. Signal Process. 159 (2021) 107827.

[19] E. Gourc, G. Michon, S. Seguy, A. Berlioz, Experimental investigation and design optimization of targeted energy transfer under periodic forcing, J. Vibr. Acoust. 136 (2014).

[20] T. Li, S. Seguy, A. Berlioz, Dynamics of cubic and vibro-impact nonlinear energy sink: Analytical, numerical, and experimental analysis, J. Vibr. Acoust. 138 (2016).

[21] E. Gourc, G. Michon, S. Seguy, A. Berlioz, Targeted energy transfer under harmonic forcing with a vibro-impact nonlinear energy sink: Analytical and experimental developments, J. Vibr. Acoust. 137 (2015).

[22] T. Li, S. Seguy, A. Berlioz, On the dynamics around targeted energy transfer for vibro-impact nonlinear energy sink, Nonlinear Dynam. 87 (2017) 1453–1466.

[23] T. Li, C.-H. Lamarque, S. Seguy, A. Berlioz, Chaotic characteristic of a linear oscillator coupled with vibro-impact nonlinear energy sink, Nonl. Dyn. 91 (2018) 2319–2330.

[24] T. Li, E. Gourc, S. Seguy, A. Berlioz, Dynamics of two vibro-impact nonlinear energy sinks in parallel under periodic and transient excitations, Int. J. Non-Linear Mech. 90 (2017) 100–110.

[25] Yimin Wei, Sha Wei, Qianlong Zhang, Xinjian Dong, Zhike Peng, Wenming Zhang, Targeted energy transfer of a parallel nonlinear energy sink, Appl. Math. Mech. 40 (2019) 621–630.

[26] Y.M. Wei, X.J. Dong, P.F. Guo, Z. Peng, W. Zhang, Enhanced targeted energy transfer by vibro impact cubic nonlinear energy sink, Intl. J. Appl. Mech. 10 (2018) 1850061.

[27] Zhenhang Wu, Manuel Paredes, Sébastien Seguy, Targeted energy transfer in a vibro-impact cubic NES: Description of regimes and optimal design, J. Sound Vib. 545 (2023) 117425.

[28] Larissa Serdukova, Rachel Kuske, Daniil Yurchenko, Fundamental competition of smooth and non-smooth bifurcations and their ghosts in vibro-impact pairs, Nonlinear Dynam. (2022) https://link.springer.com/article/10.1007/s11071-022-08152-5.

[29] Mario Di Bernardo, Christopher J. Budd, Alan R. Champneys, Piotr Kowalczyk, Piecewise-smooth dynamical systems theory and applications, in: Applied Mathematical Sciences (Switzerland), 2008.

[30] Albert C.J. Luo, Yu Guo, Vibro-Impact Dynamics, John Wiley & Sons Ltd, Oxford, UK, 2013.

[31] Larissa Serdukova, Rachel Kuske, Daniil Yurchenko, Stability and bifurcation analysis of the period-T motion of a vibroimpact energy harvester, Nonlinear Dynam. 98 (3) (2019) 1807–1819.

[32] Larissa Serdukova, Rachel Kuske, Daniil Yurchenko, Post-grazing dynamics of a vibro-impacting energy generator, J. Sound Vib. 492 (3) (2021) 115811.